Disruption of glycolytic flux is a signal for inflammasome signaling and pyroptotic cell death

Laura E. Sanman[1], Yu Qian[4], Nicholas A. Eisele[3], Tessie M. Ng[3], Wouter A. van der Linden[2], Denise M. Monack[3], Eranthie Weerapana[4], and Matthew Bogyo[1,2,3]

Departments of [1]Chemical and Systems Biology, [2]Pathology, and [3]Microbiology and Immunology, Stanford University School of Medicine, Stanford CA 94035 USA

[4]Department of Chemistry, Boston College, Chestnut Hill MA 02467 USA

Correspondence should be addressed to mbogyo@stanford.edu

Abstract

When innate immune cells such as macrophages are challenged with environmental stresses or infection by pathogens, they trigger the rapid assembly of multi-protein complexes called inflammasomes that are responsible for initiating pro-inflammatory responses and a form of cell death termed pyroptosis. We describe here the identification of an intracellular trigger of NLRP3-mediated inflammatory signaling, IL-1β production and pyroptosis in primed murine bone marrow-derived macrophages that is mediated by disruption of glycolytic flux. This signal results from a drop of NADH levels and induction of mitochondrial ROS production and can be rescued by addition of products that restore NADH production. This signal is also important for host cell response to the intracellular pathogen *Salmonella typhimurium*, which can disrupt metabolism by uptake of host cell glucose. These results reveal an important inflammatory signaling network used by immune cells to sense metabolic dysfunction or infection by intracellular pathogens.

Introduction

Inflammation is an immunological process required for an organized response to infection, injury, and stress. Because excessive inflammation can be damaging, its initiation is highly regulated. Innate immune cells such as macrophages have evolved sensors of pathogens and homeostatic perturbations which, when activated, induce an immune response[1]. Amongst these sensors are Nod-like receptors (NLRs), which are activated in response to a diverse set of pathogen-associated molecular patterns (PAMPs) and danger-associated molecular patterns (DAMPs). Activated NLR proteins recruit and facilitate activation of the protease caspase-1 either directly, through caspase activation and recruitment domain (CARD) interactions, or indirectly, through the adaptor apoptosis-associated speck-like protein containing a CARD (ASC; also known as *Pycard*). The resulting macromolecular complex is referred to as the inflammasome[2]. The inactive precursor of the cytokine interleukin-1β (pro-IL-1β) is also recruited to the inflammasome complex, where proteolysis by caspase-1 induces activation and secretion of the bioactive cytokine, further promoting inflammation. In addition to cytokine maturation, inflammasome formation and caspase activation are associated with a pro-inflammatory form of cell death termed pyroptosis[3]. This form of cell death results in lytic release of cytosolic contents and other pro-inflammatory factors such as interleukin-1α and high-mobility group protein B1 (HMGB1), which are potent inducers of inflammation[1,4].

Diverse activation signals have been reported as triggers of NLR signaling. For example, the NLR AIM2 is activated by cytosolic double-stranded DNA[2,5-7], a structural feature associated with infections with pathogens and not found in healthy host cells[3,6,8]. The NLR NLRP3 is a sensor of a wide variety of PAMPs and DAMPs but the unifying mechanism of its disparate activators is not understood[9]. Furthermore, while the NLRP3 signaling pathway can be activated

by a variety of both gram-positive and gram-negative bacteria, the mechanism by which these pathogens induce inflammasome signaling through this receptor is often unclear[10]. Specifically, effective defense against *Salmonella typhimurium (S. typhimurium)* requires NLRP3[11], yet the mechanism by which the pathogen activates this pathway remains unknown.

Here, we report a small molecule, GB111-NH_2, that induces NLRP3 inflammasome formation, caspase-1 activation, IL-1β secretion, and pyroptotic cell death in bone marrow-derived macrophages (BMDM). Using chemical proteomics, we identify the glycolytic enzymes GAPDH and α-enolase as the phenotypically relevant targets of this molecule. Facilitating TCA metabolism downstream of glycolysis by addition of pyruvate or succinate blocked the effects of the compound. We find that *S. typhimurium* infection, like direct chemical inhibition of the glycolytic enzymes, reduced glycolytic flux and that restoring metabolism downstream of glycolysis also prevented *S. typhimurium*-induced inflammasome formation, IL-1β secretion, and pyroptosis. We find that glycolytic disruption induced by either the small molecules or *S. typhimurium* infection impaired NADH production, resulting in formation of mitochondrial ROS that were essential for NLRP3 inflammasome activation. Therefore, disruption of glycolytic flux is a biologically relevant trigger of NLRP3 inflammasome activation that is mediated by mitochondrial redox changes, revealing a mechanistic link between cellular metabolism and initiation of inflammation.

Results

Identification of a small molecule activator of inflammasome formation and pyroptosis

While screening peptide-based compounds for their effects on inflammasome signaling, we identified one compound, GB111-NH_2[12,13] (Figure 1A), that was sufficient to induce caspase-1

activation in LPS-primed bone marrow-derived macrophages. We measured caspase-1 activation by monitoring conversion of procaspase-1 to the mature p10 form by Western blot and, in parallel, by labeling BMDM with the caspase-1-selective activity-based probe (ABP), AWP28[14] (Figure 1B). In addition to producing active caspase-1, we found that GB111-NH_2-treated BMDMs secreted the cytokine IL-1β in a dose-dependent manner (Figure 1C). Western blot analysis confirmed that secreted IL-1β was primarily the bioactive p17 form (Figure 1 - figure supplement 1) that is generated by active caspase-1.

By fluorescence microscopy, we observed formation of foci containing the inflammasome adaptor ASC and active caspase-1 in GB111-NH_2-treated BMDMs (Figure 1D). Formation of these foci was dependent on NLRP3 and ASC but not caspase-1, caspase-11, NLRC4, or AIM2 (Figure 1E-F). We observed that GB111-NH_2 induced a similar level of IL-1β secretion as the NLRP3 stimuli ATP and nigericin (Figure 1G) and that the absence of NLRP3 completely abrogated IL-1β secretion induced by GB111-NH_2 treatment. The absence of other NLRs, specifically NLRC4 and AIM2, had no effect on IL-1β secretion (Figure 1H). Taken together, these data indicate that GB111-NH_2 induces caspase-1 activation and IL-1β secretion solely through the NLRP3 inflammasome, acting as an activating 'Signal II' for the canonical NLRP3 pathway[2].

In order for 'Signal II' to activate the NLRP3 inflammasome, BMDM must first be primed by a 'Signal I' such as LPS. LPS priming induces NF-κB-dependent transcription of pro-inflammatory genes such as IL-1β and inflammasome-independent secretion of pro-inflammatory cytokines such as IL-6 and TNF-α[2]. We measured lysate protein levels by Western blotting and supernatant cytokine levels by ELISA in BMDM treated as in previously described experiments; first primed for 3 hours with LPS and then treated for 2 hours with GB111-NH_2.

We observed the appearance of pro-IL-1β upon LPS priming (Figure 1I) but there was no effect of GB111-NH_2 on either IL-1β protein levels in BMDM that had received LPS priming (Figure 1C, Figure 1G). In addition, IL-6 secretion decreased with increasing dose of GB111-NH_2 and TNF-α secretion was unaffected by GB111-NH_2 (Figure 1 - figure supplement 2). Therefore, GB111-NH_2 does not have a direct effect on Signal I, but functions predominantly as a Signal II for the NLRP3 inflammasome.

Macrophages containing active inflammasome complexes often rapidly die by a pro-inflammatory process called pyroptosis[3]. We observed features of this form of cell death in GB111-NH_2-treated BMDM, including release of the intracellular enzyme lactate dehydrogenase (LDH) (Figure 1J), and foci of caspase-1 activity in propidium iodide (PI) and Annexin V (AnnV) positive cells (Figure 1K). These data confirm that GB111-NH_2 is a small molecule activator of the NLRP3 inflammasome that also triggers pyroptotic cell death.

Identification of the phenotypically relevant targets of GB111-NH_2

Given that GB111-NH_2 is chemically distinct from other known activators of NLRP3 and easily modifiable, we wanted to use it as a tool to identify protein targets that are involved in triggering this pro-inflammatory response. To accomplish this, we first conducted a small structure-activity relationship (SAR) study in which we synthesized a series of analogs of GB111-NH_2 to identify compounds that could be used for affinity isolation of labeled targets. We identified a number of modifications to the primary compound scaffold that resulted in loss of activity (Figure 2A), suggesting that the effects of the parent compound are likely dictated by affinity to specific protein targets. Importantly, our SAR efforts identified both an inactive analog (GB-IA) as well as an azide-containing analog (az-GB) that retained the inflammasome-activating ability of

GB111-NH_2 (Figure 2A, Figure 2-figure supplement 1). We used this azide analog as a probe to identify potential protein targets using Click chemistry to attach a fluorescent tag (Figure 2-figure supplement 1) or affinity tag (biotin) to labeled target proteins. The choice of this probe does limit identification to covalent binding partners. However, because removal of the AOMK electrophile from GB111-NH_2 (compound 2) resulted in loss of the ability of the compound to induce IL-1β secretion, we reasoned that the compound likely acted through covalent modification of its relevant targets.

We conducted a proteomic study in which we pre-treated BMDMs with either active or inactive analogs of GB111-NH_2, labeled with the az-GB probe, reacted the resulting lysates with alkyne-biotin and identified affinity isolated targets using multidimensional protein identification technology (MudPIT)[15] (Figure 2B). By using active and inactive compounds in our pretreatment (GB111-NH_2 and GB-IA, respectively), we could identify labeled proteins that were lost by pretreatment with the active compound but not the inactive control. Employing this strategy, we obtained a short list of potentially relevant binding partners (Supplementary files 1-3). Interestingly, this list included proteins critical to cellular metabolism and homeostatic maintenance.

Inhibition of glycolytic enzymes activates the NLRP3 inflammasome and induces pyroptosis

To determine which of the potential protein targets of GB111-NH_2 were responsible for its' phenotypic effects, we first tested whether reported selective inhibitors of several of the identified targets mimicked the effects of GB111-NH_2. Based on our target list (Supplementary file 3), we selected the compounds Atpenin A5[16] (AA5; inhibitor of succinate dehydrogenase in

149 the TCA cycle), 6-aminonicotinamide[17] (6AN; inhibitor of 6-phosphogluconate dehydrogenase
150 in the pentose phosphate pathway), koningic acid[18] (KA; inhibitor of GAPDH in glycolysis) and
151 ENOblock[19] (EB; inhibitor of α-enolase in glycolysis). We tested these compounds for their
152 effects on LPS-primed BMDM and found that only inhibitors of the glycolytic enzymes
153 glyceraldehyde-3-phosphate dehydrogenase (GAPDH) and α-enolase induced IL-1β secretion,
154 inflammasome formation, and caspase-1 processing (Figure 3A-C). We chose concentrations of
155 each inhibitor based of literature descriptions of concentrations at which targets should be
156 completely inhibited[16-19]. Mass spectrometry results demonstrated that GB111-NH_2 also bound
157 to lysosomal cysteine cathepsins (Supplementary file 2), though not in the expected pattern. To
158 rule out a mode of action based on cathepsin inhibition, we tested the established cathepsin
159 inhibitors leupeptin, E-64d, and Ca074Me and found that they did not induce caspase-1
160 activation in BMDM (Figure 3-figure supplement 1). These data indicate that the phenotypically
161 relevant targets of GB111-NH_2 are the glycolytic enzymes GAPDH and α-enolase.
162 The GAPDH and α-enolase inhibitors KA and EB failed to induce inflammasome
163 formation in cells that lack *Pycard* or *Nlrp3* (Figure 3D), induced IL-1β secretion in a dose-
164 dependent manner that was also NLRP3-dependent (Figure 3E, Figure 3 – figure supplement 2),
165 and had no effect on pro-IL-1β or NLRP3 levels in LPS-primed BMDM (Figure 3A, Figure 3F).
166 These data demonstrate that structurally dissimilar inhibitors of either GAPDH or α-enolase
167 activate the canonical NLRP3 inflammasome pathway similarly to GB111-NH_2.
168 To further confirm the targets of GB111-NH_2, we measured the ability of the parent
169 compound and its analogs to covalently bind and inhibit the activity of the identified glycolytic
170 enzyme targets. To test if our compounds covalently bound to GAPDH and α-enolase, we
171 incubated recombinant GAPDH and α-enolase with our az-GB probe, used Click chemistry to

attach TAMRA-alkyne to the az-GB probe, and analyzed reaction mixtures by fluorescent scanning of SDS-PAGE gels. We observed probe labeling of both GAPDH and α-enolase, indicating that the az-GB probe covalently binds to both enzymes (Figure 4A-B, Figure 4 – figure supplement 1). Pretreatment with GB111-NH_2 blocked az-GB binding to both GAPDH and α-enolase in a dose-dependent manner, indicating that both compounds bind to similar sites on their enzyme targets. The GB111-NH_2 analog containing a more reactive phenoxymethylketone electrophile (compound 6), which also induced IL-1β secretion more potently in cells than GB111-NH_2, also blocked az-GB binding to both GAPDH and α-enolase at lower concentrations compared to GB111-NH_2. Importantly, the analogs that did not induce IL-1β secretion in BMDM, compound 2 (which lacks the AOMK electrophile) and GB-IA (which lacks the carboxybenzyl cap of GB111-NH_2), did not compete for az-GB binding to GAPDH and α-enolase. We did observe some labeling of GAPDH and α-enolase by TAMRA-alkyne independent of the az-GB probe, which is potentially due to the ability of alkynes to function as cysteine electrophiles[20].

az-GB probe binding to both enzymes was blocked by the cysteine-alkylating compound N-ethylmaleimide (NEM), and by KA and EB (for GAPDH and α-enolase, respectively), suggesting that binding was dependent on enzyme activity and was mediated by reaction with key reactive cysteines (Figure 4 – figure supplement 1). To further investigate the proposed covalent interaction of GB111-NH_2 with reactive cysteine residues in GAPDH and α-enolase, we performed competition studies with the general cysteine reative probe iodoacetamide fluorescein (IAF). IAF labeled both GAPDH and α-enolase, consistent with previous reactive cysteine profiling data demonstrating that the catalytic Cys 152 of GAPDH is highly reactive and Cys 388, an active-site proximal cysteine of α-enolase, is also reactive[21]. NEM potently blocked

IAF labeling, confirming that IAF was reacting with cysteine residues in GAPDH and α-enolase. Importantly, GB111-NH_2 also competed for IAF labeling, indicating that it covalently binds these same reactive cysteines (Figure 4C-D).

Modification of the active-site cysteine of GAPDH and the active site-proximal Cys 388 of α-enolase have both been shown to potently impair enzyme activity[22,23]. To confirm that binding of our compounds to these enzymes also inhibits enzyme activity, we performed substrate assays with recombinant GAPDH and α-enolase and found that GB111-NH_2 dose-dependently inhibited turnover of the respective substrates, glyceraldehyde-3-phosphate and 2-phosphoglycerate (Figure 4E). GB-IA did not significantly inhibit GAPDH but did exhibit modest inhibitory activity towards α-enolase. GB111-NH_2 also showed time-dependent inhibition of GAPDH and α-enolase activity (Figure 4F), suggesting that it is acting as an irreversible inhibitor[24]. Taken together, these data indicate that GB111-NH_2 binds covalently to reactive cysteine residues in both GAPDH and α-enolase and that binding to these cysteine residues inhibits enzyme activity.

Because GAPDH activity was recently shown to determine flux through aerobic glycolysis[25], we hypothesized that our compounds were activating NLRP3 by disrupting glycolytic flux. Productive glycolysis results in conversion of NAD+ to NADH, secretion of lactate, and ATP production (Figure 5A). To first test the hypothesis that GB111-NH_2, KA, and EB block glycolytic flux we measured the ratio of NAD+/NADH, lactate production, and intracellular ATP concentration in inhibitor-treated BMDM. LPS stimulation, which up-regulates glycolysis in macrophages[26], resulted in an increase in NADH levels (demonstrated by a decrease in NAD+/NADH ratio) and an increase in lactate secretion (Figure 5B-D). GB111-NH_2 treatment completely blocked the lactate and NADH production induced by LPS stimulation,

indicating that it directly impaired LPS-induced glycolytic flux (Figure 5B-D). ATP production was also significantly impaired in LPS-primed BMDM upon GB111-NH_2 treatment (Figure 5E). Notably, treatment with the NLRP3 activator nigericin did not reduce NADH levels (Figure 5B, Figure 5 – figure supplement 1), indicating that the metabolic disruption that we observed with GB111-NH_2 is not a general feature of inflammasome activation and cell death. The GAPDH and α-enolase inhibitors KA and EB also affected metrics of glycolytic flux (Figure 5B-D). Finally, GB111-NH_2 suppressed the increase in extracellular acidification rate (ECAR) induced by glucose stimulation (Figure 5F). 2DG, a glycolytic inhibitor that targets hexokinase, did not dramatically impair glycolytic flux (as measured by NADH production and lactate secretion) and did not induce inflammasome formation (Figure 5-figure supplement 2). This indicates that severe limitation of glycolytic flux is required to activate the NLRP3 inflammasome. Furthermore, these results are in accord with recent studies showing that inhibiting GAPDH, and not enzymes in upper glycolysis, is flux-limiting in highly glycolytic cells[27]. Inhibitors of the TCA cycle and pentose-phosphate pathways (AA5 and 6-AN, respectively), carbohydrate metabolism pathways that are closely tied to glycolysis, also had no effect on lactate secretion or NADH production in LPS-primed BMDM and did not induce IL-1β secretion (Figure 3A, Figure 5C).

We hypothesized that, due to the dependence of macrophages on glycolytic metabolism[28], disruption of this pathway would create a metabolic signal that is responsible for activating NLRP3. We hypothesized that supplementation of downstream metabolites of glycolysis would restore partial metabolic function and block the NLRP3-activating signal. When we cultured GB111-NH_2-treated BMDMs with cell-permeable versions of the terminal metabolite of glycolysis, pyruvate, or the TCA cycle metabolite succinate, we observed a dramatic reduction in

241 the number of inflammasome foci that formed (Figure 6A). A structurally related metabolite,
242 lactate, which does not fuel the TCA cycle, did not reduce GB111-NH_2-induced NLRP3
243 inflammasome formation (Figure 6A). Doubling the media concentration of L-glutamine, a
244 metabolite that can be converted into succinate via anaplerosis[29], significantly reduced the
245 number of inflammasomes that formed. Complete removal of L-glutamine from media sensitized
246 BMDM to GB111-NH_2-induced inflammasome formation (Figure 6B). Taken together, this
247 indicates that levels of glycolytic products that fuel downstream metabolism mediate
248 inflammasome induction in response to glycolytic disruption.
249 In addition to preventing inflammasome formation, supplementation of the glycolytic
250 product pyruvate resulted in significant reductions in caspase-1 activation, IL-1β secretion, and
251 cell death induced by GB111-NH_2. Pyruvate supplementation had no effect on inflammasome
252 signaling induced by the NLRP3 activators ATP and nigericin (Figure 6C-E), indicating that
253 pyruvate does not impair NLRP3 inflammasome signaling by a nonspecific mechanism.
254 Pyruvate treatment also blocked inflammasome formation induced by KA and EB (Figure 6F)
255 and restored NADH and ATP production in the treated cells (Figure 6G-H).
256
257 **NLRP3 inflammasome activation induced by GB111-NH_2 is mediated by NAD+/NADH**
258 **imbalance and mitochondrial ROS**
259 We hypothesized that changes in the NAD+/NADH ratio or a drop in ATP concentration could
260 serve as a secondary signal that connects glycolytic disruption to NLRP3 inflammasome
261 formation. To test whether either of these signals is important, we manipulated the
262 NAD+/NADH and ATP levels downstream of glycolysis by chemically blocking specific
263 components of the TCA cycle and oxidative phosphorylation. We first treated LPS-primed

BMDM with GB111-NH_2 and pyruvate to block glycolysis and stimulate downstream metabolism. We then added the succinate dehydrogenase (TCA cycle enzyme) inhibitor AA5[16] to reduce NADH levels, the Complex I inhibitor rotenone to increase NADH levels and reduce ATP production, or the ATP synthase inhibitor Oligomycin A to only inhibit ATP synthesis by oxidative phosphorylation (Figure 7A-B). We found that AA5 addition partially reversed the protection conferred by pyruvate, as demonstrated by an increase in the number of inflammasome complexes. Rotenone treatment suppressed inflammasome formation more than pyruvate alone. Oligomycin A induced a small but statistically insignificant increase in the number of inflammasomes that formed (Figure 7C). The number of inflammasomes positively correlated with a drop in NADH production (an increase in NAD+/NADH ratio) (Figure 7D), while ATP concentration exhibited no correlation with the numbers of inflammasomes (Figure 7 – figure supplement 1). Interestingly, rotenone treatment was sufficient to completely abrogate inflammasome formation induced by GB111-NH_2 (Figure 7E), conditions under which we also observed a significant decrease in the NAD+/NADH ratio (Figure 7F). These data suggest that the inability to produce NADH, and not ATP, is predictive of NLRP3 inflammasome formation upon glycolytic disruption by GB111-NH_2. It should be noted, however, that the α-enolase inhibitor EB did not induce a significant NAD+/NADH ratio defect (Figure 5), suggesting that either EB induces inflammasome activation through a distinct mechanism from GB111-NH_2 and KA, or that there are additional universal signals responsible for inflammasome activation downstream of glycolytic disruption.

Mitochondrial ROS and K+ efflux are proposed to be unifying signals preceding NLRP3 inflammasome formation[30,31]. Therefore, we wanted to determine whether either of these signals is relevant to NLRP3 inflammasome activation induced by disruption of glycolysis. We stained

BMDM with MitoSOX, a dye that reports accumulation of mitochondrial ROS, and observed that GB111-NH_2 induced an increase in cellular MitoSOX fluorescence that was abrogated by addition of pyruvate (Figure 7G). We also found that the ROS scavenger 4-hydroxyTEMPO (4-HT) prevented GB111-NH_2-induced caspase-1 cleavage and activation (Figure 7H). Addition of extracellular K+, in contrast, did not reduce the number of inflammasome foci in GB111-NH_2-treated BMDMs (Figure 7I) or impair GB111-NH_2-induced cell death (Figure 7 – figure supplement 2), indicating that mitochondrial ROS, but not K+ efflux, is required for GB111-NH_2-induced NLRP3 activation and pyroptosis.

Salmonella typhimurium infection induces NLRP3 inflammasome formation by disruption of host cell metabolism

We and others have shown that the intracellular pathogen *Salmonella typhimurium* (*S. typhimurium*) requires glucose and its own glycolytic enzymes for intracellular replication[32,33]. In addition, host defense against *S. typhimurium* requires the NLRC4 and NLRP3 inflammasomes[11]. While it is clear that *S. typhimurium* flagellin and type 3 secretion system proteins activate NLRC4 via NAIP proteins[34], the mechanism by which NLRP3 is activated is not well understood. We hypothesized that *S. typhimurium* infection may stimulate NLRP3 through disruption of host cell metabolic pathways by co-opting cellular resources during intracellular replication. To test this notion, we infected naïve BMDM with *S. typhimurium* grown to stationary phase (conditions that lead to NLRP3-dependent inflammasome activation[11]). In this infection model, inflammasome complexes begin forming at ~11 hours post-infection and progressively accumulate. We confirmed that infection with either wildtype *S. typhimurium* or *S. typhimurium* lacking the SPI-1 secretion system (which genetically limits *S. typhimurium* to activating NLRP3) induced inflammasome formation (Figure 8A-B). In addition, the percentage

of cells with ASC foci was similar in magnitude to GB111-NH_2 and alum treatment but lower than nigericin, ATP, or log phase *S. typhimurium* stimulation (Figure 8C). Using this infection model, we assessed the extent to which intracellular *S. typhimurium* utilize host cell glucose by culturing infected BMDM with the fluorescent glucose analog 2-(*N*-(7-nitrobenz-2-oxa-1,3-diazol-4-yl)amino)-2-deoxyglucose (2-NBDG). We lysed infected BMDM at 5 hours post-infection (while bacteria are still intracellular), harvested the bacterial fraction of BMDM lysates, and measured 2-NBDG fluorescence. We observed fluorescent signal that was dependent on infection in 2-NBDG-treated macrophages, indicating that the bacterial fraction took up the fluorescent glucose analog from the host cell (Figure 8D). We also fixed uninfected and infected 2-NBDG-treated BMDM and analyzed the pattern of 2-NBDG fluorescence by confocal microscopy. We observed the presence of strongly 2-NBDG fluorescent punctae that resemble *S. typhimurium* and colocalize with Hoechst stain (which stains both host cell and bacterial DNA) in infected BMDM. Furthermore, we quantified the portions of cytosol that were not Hoechst-positive and observed a significant decrease in 2-NDBG fluorescence in the cytosol of infected BMDM compared to uninfected BMDM (Figure 8E). These data indicate that intracellular *S. typhimurium* derive glucose from host macrophages and reduce host glucose availability.

We measured glycolytic flux in infected BMDM to assess the effect of limited glucose availability on the host macrophages. Importantly, as observed for GB111-NH_2 treatment, we observed reduced production of NADH and lactate (Figure 8F-H) that correlated with the multiplicity of infection and magnitude of inflammasome formation in host cells (Figure 8A, Figure 8F-H). These metabolic defects appeared on a similar timescale as initiation of NLRP3 inflammasome formation, suggesting that infection with *S. typhimurium* has a direct effect on glycolytic flux in host cells.

Consistent with our findings using glycolytic inhibitors, we also observed that supplementation of cells with the glycolytic end product pyruvate significantly reduced inflammasome formation, IL-1β secretion, and cell death induced by *S. typhimurium* infection (Figure 9A-D). Pyruvate was effective at blocking inflammasome formation in BMDMs infected with both wildtype *S. typhimurium* and *S. typhimurium* defective for the SPI-1 secretion system (Figure 9 – figure supplement 1). Notably, pyruvate did not completely block ASC focus formation, IL-1β secretion, and death induced by *S. typhimurium* infection, which could be due to compensatory activation of other inflammasomes such as the non-canonical caspase-11 inflammasome[35], or because *S. typhimurium* could also partially co-opt host pyruvate.

We did not observe inflammasome focus formation in *Nlrp3* -/- BMDMs upon infection with stationary phase *S. typhimurium*. In contrast, *Nlrc4* -/- BMDMs had a similar number of inflammasome foci upon infection as wildtype macrophages (Figure 9E). Pyruvate did not prevent inflammasome formation or cell death induced by infection with *S. typhimurium* in log phase growth (Figure 9 – figure supplement 2), an infection model that activates the NLRC4 inflammasome. We also verified that pyruvate was not blocking inflammasome formation by inhibition of bacterial replication using both an intracellular replication reporter plasmid[36] and by monitoring bacterial replication by microscopy (Figure 9F-G). Reporter plasmid expression over the course of the intracellular replication assay indicates that intracellular *S. typhimurium* are viable in BMDM cultured in DMEM with or without pyruvate[36]. *In vitro* replication assays demonstrated that *S. typhimurium* grew at a similar rate in minimal media with glucose or pyruvate as a carbon source (Figure 9H), further indicating that pyruvate supplementation affects host cell recognition of intracellular bacteria rather than bacterial dynamics. Importantly, we found that the NAD+ consumption rate increased upon pyruvate treatment (Figure 9I), indicating

induction of productive metabolism downstream of glycolysis in infected BMDMs. Taken together, these data indicate that glycolytic perturbation is a mechanism by which innate immune cells sense altered homeostasis during *S. typhimurium* infection and induce a pro-inflammatory response via NLRP3 inflammasome formation and pyroptotic cell death.

Discussion

The inflammasome is a multiprotein complex that forms in response to various pathogen- and danger-associated signals. Formation of the inflammasome leads to processing and secretion of pro-inflammatory cytokines to activate the immune system[2,37]. While inflammasome formation and pyroptotic cell death are critical for fighting infection and also contribute to inflammation in diseases including type II diabetes, obesity, and atherosclerosis[38-40], the signals that trigger caspase-1 activation remain poorly understood. In this study, we used a small molecule, GB111-NH_2, to identify two glycolytic enzymes that regulate inflammasome formation. When functionally blocked, innate immune cells sense metabolic perturbation as a danger signal, resulting in inflammasome formation, caspase-1 activation, and cytokine secretion. Our results using this molecule and other established inhibitors of these enzymes suggest that disrupting glycolytic flux serves as a trigger for inflammation and cell death in macrophages. Disturbance of glycolytic flux by the intracellular pathogen *S. typhimurium* similarly results in inflammasome formation and pyroptotic cell death in an effort to clear the pathogen. Restoration of metabolism downstream of glycolytic disruption by GB111-NH_2 or *S. typhimurium* infection was sufficient to abrogate the inflammasome response by restoring NADH production and preventing mitochondrial ROS production.

Though the enzymes and metabolites involved in glycolysis are well established, the specific mechanisms that limit glycolytic flux are not well understood. The irreversible reactions within glycolysis, catalyzed by hexokinase, phosphofructokinase, and pyruvate kinase, were historically thought to be rate limiting. However, recent metabolite flux analyses have also suggested that flux through GAPDH, the enzyme separating upper and lower glycolysis, is rate-limiting under nutrient-rich conditions[27]. Under similar conditions, we also observed that targeting GAPDH or enzymes in lower glycolysis is sufficient to disrupt glycolytic flux and activate the NLRP3 inflammasome. Conversely, targeting entry into glycolysis using 2DG was not sufficient to disrupt glycolysis in highly glycolytic cells, as has previously been reported[25], or to activate NLRP3. This reaffirms previous observations that the pre-existing metabolic state of the cell and the point of intervention are equally important for effectively limiting glycolytic flux[41]. Disruption of glycolytic flux led to an NAD+/NADH imbalance and induced mitochondrial ROS accumulation, which has been shown here and elsewhere[30,42] to activate the NLRP3 inflammasome (Figure 10).

During infection with *S. typhimurium*, inflammasome activation is an especially important mechanism of host response because, though it kills the host cell, it initiates inflammatory signals that activate the immune system and combat infection[10]. Two inflammasome complexes, NLRP3 and NLRC4, are required to fully combat infection[11]. The NLRC4 inflammasome responds to a clear pathogen-associated molecular pattern presented by *S. typhimurium*—cytosolic flagellin and type 3 secretion system components[34]. Here we provide evidence that NLRP3 activation results in response to another effect of *S. typhimurium* colonization of the host cell, namely disruption of host cell glycolytic metabolism. This could explain a recent study showing that mutants of *S. typhimurium* defective for the TCA cycle

enzyme aconitase induce a more rapid NLRP3-dependent immune response *in vivo*[43]. We reason that aconitase deficiency would force *S. typhimurium* to rely even more heavily on glycolysis to survive within the host. These *S. typhimurium* mutants would likely disrupt cellular glycolysis more quickly and thus activate NLRP3 more rapidly. It is also interesting that, in long-term models of *S. typhimurium* infection, the bacteria preferentially resides within alternatively activated or 'M2' macrophages, which primarily utilize oxidative metabolism rather than glycolysis[44]. Thus, the macrophages in which *Salmonella* survives the longest are those in which host metabolic pathways are minimally perturbed, enabling prolonged infection without invoking an inflammasome response.

These findings additionally shed light on recent work highlighting the connection between metabolic changes and immune system activation[45-47]. For example, metabolic sensing by immune cells has been recently shown to drive NLRP3-dependent IL-1β release and inflammation in diseases ranging from type II diabetes and obesity to Muckle-Wells syndrome[38,48], though the specific mechanisms driving macrophage and NLRP3 activation in these diseases have remained unclear. We speculate that, since glucose metabolism is often impaired in these diseases, glycolytic impairment may be the mechanism driving NLRP3-dependent inflammation. Restoring glycolysis or downstream TCA cycle metabolism through supplementation with specific metabolites or activation of glycolytic enzymes could be therapeutically useful for dampening inflammation and associated immunopathology.

In summary, our results suggest that inhibition of glycolysis creates a unique metabolic state that activates the NLRP3 inflammasome. They suggest that innate immune cells sense perturbed metabolite production and flux through the glycolytic pathway, in turn activating NLRP3 to initiate inflammatory responses. Inhibitors of flux-limiting enzymes and *S.*

typhimurium effectively limited glycolysis through distinct mechanisms, each resulting in NLRP3-mediated inflammasome formation and pyroptosis. Glycolytic disruption may be a broadly relevant mechanism of NLRP3 activation triggered in response to metabolic parasitism by microbes. Moreover, this pathway may also provide novel avenues for treating diseases in which NLRP3-driven inflammation results in pathology.

Materials and Methods

Compound information

See below for synthesis and characterization of GB111-NH_2 and analogs. NMR spectra were recorded on a Varian 400 MHz (400/100) or a Varian Inova 500 MHz (500/126 MHz) equipped with a pulsed field gradient accessory. Chemical shifts (∂) are reported in parts per million (ppm) downfield from tetramethylsilane and are reference to the residual protium signal in the NMR solvents. Data are reported as follows: chemical shift, multiplicity (s=singlet, d=doublet, t=triplet, m=multiplet and q=quartet), coupling constant (J) in Hertz (Hz) and integration. E64d (Enzo Lifesciences), leupeptin (Sigma), CA074Me (EMD Millipore), LPS from *E. coli* 0111:B4 (Sigma), 6-aminonicotinamide (Santa Cruz Biotech), Imject Alum (Pierce), Atpenin A5 (Santa Cruz Biotech), N-ethylmaleimide (Sigma), rotenone (Sigma), oligomycin A (Cayman Chemical), nigericin (Cayman Chemical), MitoSOX (Life Technologies), ATP (Sigma), and koningic acid (Adipogen) were purchased from commercial sources, dissolved in vendor-recommended solvents, and used without further purification. ENOblock [19] was a generous gift from Dr. Darren Williams.

Bacterial Strains

Strains used in this study were *Salmonella typhimurium* NCTC 12023 and ATCC SL1344. Bacteria were grown in LB at 37C with aeration and supplemented with 0.2% arabinose if needed to induce expression of fluorescent proteins.

Mice

Mice lacking *Pycard, Nlrp3, Nlrc4,* and *Aim2* have been previously described[8,11,49,50]. Mice were maintained following guidelines approved by the Stanford University School of Medicine Administrative Panel on Laboratory Animal Care.

Cell Culture Protocols

BMDM were isolated by culturing mouse bone marrow in DMEM with 2 mM L-glutamine, 10% FBS, and 10 ng/mL recombinant mouse M-CSF (eBioscience) for 5 days in petri dishes. After 5 days, the cell monolayer was washed several times with sterile PBS to remove cell debris and then the BMDM harvested using CellStripper. BMDM were then plated for experiments, frozen, or cultured for up to a week. One day prior to treatment, cells were seeded in 6 well plates at a density of 1-2x10^6 cells/well (or 2x10^5 cells/well of 24-well dish, or 3x10^4 cells/well of 96-well dish). C57BL/6 SV40-immortalized macrophages were cultured in RPMI with 10% FBS and 2 mM L-glutamine and were a generous gift from Petr Broz.

Replicates and Statistical Analyses

In this study, biological replicates indicate replicates of the same experiment conducted upon separately seeded cultures on separate days. Technical replicates indicate separate measurements made on cells seeded on the same day and treated simultaneously. The number of biological

replicates is indicated in the figure legends and was generally n=3. For plate reader-based assays, experiments were generally conducted in technical triplicate as recommended by assay manufacturers. For microscopy experiments, at least four fields of view were generally analyzed – covering the four quadrants of the cover slip. Within each quadrant, a field was chosen at random using the DAPI channel (to simply find a region that contained cells). Each field of view was counted as a technical replicate because it was a separate measurement of a singly seeded culture. When ascertaining whether differences between samples were statistically significant, an unpaired, two-tailed t test was used. This makes the assumptions that the two samples under analysis were approximately normally distributed and had equal variances. $p < 0.05$ was considered significant. Because measurements were taken within linear range of the detection method (i.e., below saturation and above noise for absorbance-based plate reader assay, within linear range of detector for flow cytometry measurements), etc, technical replicates should be normally distributed around the mean.

LPS Priming and Inflammasome Activation

BMDM were primed with 100 ng/mL LPS-EK (Invivogen) or LPS 0111:B4 (Sigma) in DMEM for 3hr before addition of inflammasome activating agents. GB111-NH_2 was added to LPS-primed BMDM at 10 μM (unless otherwise indicated) for inflammasome activation. The canonical NLRP3 activators ATP and nigericin were added to LPS-primed BMDM at 5 mM and 12.5 μM, respectively, typically for 1 hour. Alum (Pierce) was used at a concentration of 100 μg/mL for 5 hours.

***Salmonella typhimurium* Infections**

For stationary phase infections, *S. typhimurium* grown to stationary phase (typically overnight culture in LB) were centrifuged onto BMDM for 10min at 500g. After 1hr, medium was switched to DMEM with 100 μg/mL gentamicin sulfate to kill extracellular bacteria. After 1hr, cells were washed with plain DMEM and then incubated in DMEM with 10 μg/mL gentamicin sulfate for the remainder of the infection. For log phase infections, *S. typhimurium* in log phase growth (typically a 4hr subculture of a 1:50 dilution of an overnight culture) were centrifuged onto BMDM for 10min at 500g in antibiotic-free DMEM. Unless otherwise stated, samples were analyzed after 1 hour of log phase infection.

Probe labeling

Probes were diluted to the desired final concentration (1 μM for AWP28, 250 nM for BMV109) from a 1000x stock solution in DMSO directly in the media of the cell monolayer. Cells were labeled for the final hour of treatment at 37C prior to sample preparation and analysis. For gel labeling experiments, labeled cell monolayers were washed in PBS and lysed directly with 50 μL sample buffer. For harvested supernatants, following treatment the supernatant was removed and proteins precipitated by adding 4 equivalents of cold acetone. Samples were incubated in acetone overnight at -20C, then proteins pelleted by centrifugation for 5 minutes at 2000 rpm. Acetone was aspirated and protein pellets dried for 30 minutes at 37C before addition of sample buffer. Samples were resolved by SDS-PAGE and visualized on a Typhoon flatbed fluorescent laser scanner (GE Healthcare).

Western Blots

Following separation of samples by SDS-PAGE and transfer to 0.2 μM nitrocellulose resin (BioRad), the following antibodies were used. For cell lysates: anti-caspase-1 p10 (1:200, Santa Cruz Biotechnology #514), anti-HSP-90 (1:1000, BD Biosciences), anti-NLRP3 (1:500, R&D Systems), anti-α-tubulin (1:10000, Sigma), anti-GAPDH (1:1000, Santa Cruz Biotechnology C-9), anti-α-enolase (1:1000, Cell Signaling Technology). For cell supernatant: anti-IL-1β (1:200, Cell Signaling Technology). HRP-conjugated α-mouse and α-rabbit secondary antibodies were from GE Healthcare.

ELISA Protocols

BMDMs were seeded in triplicate in 96 well plates at a density of $3x10^4$ cells/well. Following treatment, the supernatant was removed and IL-1β, IL-6, or TNF-α release was measured using a Mouse IL-1β, IL-6, or TNF-α READY-SET-GO ELISA kits (eBioscience) according to the manufacturer's instructions.

LDH Release Assays

BMDMs were seeds in triplicate in 96 well plates at a density of $3x10^4$ cells/well. Following treatment, the supernatant was removed and the cells were lysed with 2% Triton-X-100 in D-PBS. The lysate was diluted in culture media to the original volume. LDH release was calculated as supernatant LDH activity/total LDH activity using the CytoTox 96 Assay (Promega).

Microscopy and Image Analysis

BMDMs were seeded on poly-L-lysine coated glass coverslips in 24 well plates at a density of $2x10^5$ cells/well. Following treatment and labeling with AWP28 (1 μM for final hour of

538 treatment), the cell monolayer was rinsed 3x with warm D-PBS and then fixed with 4%
539 paraformaldehyde in PBS for 15 minutes at 37C. The cells were washed with PBS and incubated
540 with anti-ASC (1:200, Santa Cruz Biotechnology N-15) primary antibody in blocking buffer (3%
541 BSA, 0.1% saponin, 0.02% sodium azide in PBS) for 30 minutes. The cells were washed 3x with
542 PBS and incubated with Alexa 647 or Alexa 594-conjugated secondary antibody (both 1:1000,
543 Invitrogen) for 30min. The cells were washed with D-PBS, mounted in Vectashield with DAPI
544 (Vector Labs), and imaged on a Zeiss LSM700 confocal microscope. Snapshots of fields were
545 taken at random (at least 4 fields/condition using a 10x or 20x air objective, typically ~2000
546 cells/condition). Nuclei were counted using the ITCN plug-in in ImageJ and inflammasome
547 (ASC and/or AWP28 positive) foci were counted using the 'Analyze Particles' function in
548 ImageJ after automated thresholding. Replicates indicate cells plated and treated on separate
549 days. For Annexin V and propidium iodide staining, AWP28 labeled cells on coverslips were
550 washed with Annexin V binding buffer (10 mM HEPES pH 7.4, 150 mM NaCl, 2.5 mM $CaCl_2$)
551 and then incubated with 1 μg/mL propidium iodide (ImmunoChemistry) and 1:50 Alexa 647
552 conjugated Annexin V (Invitrogen) in Annexin V binding buffer on ice for 30 minutes. Cells
553 were washed with Annexin V binding buffer and mounted in Vectashield (Vector Labs) for
554 immediate imaging.
555
556 **Mass- Spectrometry Sample Preparation and Analysis**
557 *Competition proteomics and sample preparation:* C57BL/6 BMDMs were seeded onto 15 cm
558 dishes ($2x10^7$ cells/dish). The number of dishes per condition was calculated such that
559 approximately 3 milligrams of protein were yielded per condition. The competition experiment
560 took place as follows: For condition 1, BMDMs were incubated with 100 ng/mL LPS for 3 hours,

after which 50 μM az-GB from 100x DMSO stock was added to culture media for 2 hours. For condition 2, BMDMs were incubated with 100 ng/mL LPS for 2 hours. 10 μM GB111-NH_2 from 1000x DMSO stock was added to the culture media for 1 hour, after which 50 μM az-GB from 100x DMSO stock was added to culture media for 2 hours. For condition 3, BMDMs were incubated with 100 ng/mL LPS for 2 hours. 50 μM GB-IA from 1000x DMSO stock was added to the culture media for 1 hour, after which 50 μM az-GB from 100x DMSO stock was added to the culture media for 2 hours. For condition 4, BMDMs were incubated with 100 ng/mL LPS for 3 hours, after which vehicle was added for 2hr. After treatment, all cells were lifted from tissue culture dishes using CellStripper (Corning Cellgro), pelleted at 1000 rpm for 5min, washed once with PBS, and lysed on ice in D-PBS containing 1% NP-40 and 0.1% SDS. Cellular debris was pelleted by centrifugation at 14000 rpm for 15min at 4C. The supernatant was removed and protein concentration determined by BCA Assay (Pierce). Protein concentrations were then normalized to 2 mg/mL in PBS with 1% SDS.

Click chemistry and streptavidin enrichment of probe-labeled proteins: Protein samples (>3 mg/condition) then underwent click chemistry. Biotin azide was added to 10 μM final concentration, fresh TCEP (Sigma) to 1 mM, TBTA (Sigma) to 100 uM, and $CuSO_4$ to 1 mM. Samples were allowed to react at room temperature for 3 hours. Proteins were then precipitated using 5 volumes -20˚C acetone. After 2 hours, protein precipitates were pelleted. The pellets were washed 4x with -20˚C acetone, air dried, and resuspended in PBS with 1.2% SDS. These solutions were incubated with 100 μL streptavidin-agarose beads (Thermo Scientific) at 4˚C for 16 hrs. The solutions were then incubated at room temperature for 2.5 hours. The beads were washed with 0.2% SDS/PBS (5 mL), PBS (3 x 5 mL), and water (3 x 5 mL). The beads were pelleted by centrifugation (1400 x g, 3 min) between washes.

584 *On-bead trypsin digestion:* The washed beads were suspended in 6 M urea/PBS (500 µL) and 10
585 mM dithiothreitol (DTT) (from 20X stock in water) and placed in a 65°C heat block for 15 mins.
586 Iodoacetamide (20 mM, from 50X stock in water) was then added and the samples were placed
587 in the dark and allowed to react at room temperature for 30 mins. Following reduction and
588 alkylation, the beads were pelleted by centrifugation (1400 x g, 3 min) and resuspended in 200
589 µL of 2 M urea/PBS, 1 mM CaCl2 (100X stock in water), and trypsin (2 µg). The digestion was
590 allowed to proceed overnight at 37 °C. The peptide digests were separated from the beads using
591 a Micro Bio-Spin column (BioRad). The beads were washed with water (2 x 50 µL) and the
592 washes were combined with the eluted peptides. Formic acid (15 µL) was added to the samples.
593 These tryptic digests were stored at -20 °C until mass spectrometry analysis.
594 *Liquid chromatography-mass spectrometry (LC-MS) analysis:* LC-MS analysis was performed
595 on an LTQ Orbitrap Discovery mass spectrometer (ThermoFisher) coupled to an Agilent 1200
596 series HPLC. Digests were pressure loaded onto a 250 µm fused silica desalting column packed
597 with 4 cm of Aqua C18 reverse phase resin (Phenomenex). The peptides were eluted onto a
598 biphasic column (100 µm fused silica with a 5 µm tip, packed with 10 cm C18 and 3 cm
599 Partisphere strong cation exchange resin (SCX, Whatman) using a gradient 5-100% Buffer B in
600 Buffer A (Buffer A: 95% water, 5% acetonitrile, 0.1% formic acid; Buffer B: 20% water, 80%
601 acetonitrile, 0.1% formic acid). The peptides were eluted from the SCX onto the C18 resin and
602 into the mass spectrometer following the four salt steps outlined in Weerapana et al (2007). The
603 flow rate through the column was set to ~0.25 µL/min and the spray voltage was set to 2.75 kV.
604 One full MS scan (400-1800 MW) was followed by 8 data dependent scans of the nth most
605 intense ions with dynamic exclusion enabled.

606 *Mass spectrometry data analysis:* The generated tandem MS data was searched using the
607 SEQEST algorithm against the human UNIPROT database. A static modification of +57 on Cys
608 was specified to account for iodoacetamide alkylation. The SEQUEST output files generated
609 from the digests were filtered using DTASelect 2.0 to generate a list of protein hits with a
610 peptide false-discovery rate of <5%.
611 When comparing results from Conditions 1-4, spectral counts were first normalized based on the
612 spectral counts of the four endogenously biotinylated mammalian proteins, pyruvate carboxylase,
613 3-methylcrotonyl CoA carboxylase, propionyl CoA carboxylase, and acetyl CoA carboxylase[51].
614 Condition 4 determined "background" levels of reactivity with alkyne-biotin. Candidate proteins
615 were those with >30 spectral counts in condition 1, >80% competition by GB111-NH_2 for az-GB
616 binding in condition 2, and less than 50% competition by GB-IA for az-GB binding in condition
617 3. Pearson correlation between enrichment in different samples and expected enrichment was
618 calculated for confidence in hit proteins.
619
620 **Enzyme Labeling Assays**
621 Recombinant GAPDH (ScienCell), α-enolase (BioVision) were diluted into assay buffer (50 mM
622 Tris-HCl pH 7.4, 1.5 mM $MgCl_2$) and incubated with inhibitor or vehicle for 30 minutes at 37C.
623 After this, az-GB (50 μM) was added for 2 hours at 37C. TAMRA-alkyne was then added under
624 previously described Click reaction conditions[52] to visualize az-GB-labeled protein. Reaction
625 mixtures were separated by SDS-PAGE and visualized on Typhoon scanner.
626
627 **Enzyme Activity Assays**

GAPDH Activity Assay: Recombinant GAPDH (0.02 units) was incubated in GAPDH Assay Buffer (ScienCell) for 30 minutes at 37C in the presence of inhibitor or vehicle. This mixture was then added to Assay buffer, which contains 6.7 mM phosphoglyceric acid, 3.3 mM L-cysteine, 117 μM β-NADH, 1.13 mM ATP, and 0.05 U 3-phosphoglycerate kinase in 150 μL. A_{340}, representing conversion of β-NADH to NAD+, was measured every minute for 30 minutes by plate reader (SpectraMax M5, Molecular Devices). Percentage inhibition was calculated as: (treatment ΔA_{340}/vehicle ΔA_{340})x100.

α-enolase Activity Assay: Approximately 0.013 units of recombinant α-enolase (MyBioSource.com) were incubated in assay buffer (50 mM Tris-HCl pH 7.4, 1.5 mM $MgCl_2$) for 30 minutes at 37C in the presence of inhibitor or vehicle. Phosphoenolpyruvate (Sigma) was added to a final concentration of 1.5 mM. A_{240}, representing conversion of phosphoenolpyruvate to 2-phosphoglycerate, was measured every minute for 30 minutes by plate reader. Percentage inhibition was calculated as: (treatment ΔA_{240}/vehicle ΔA_{240})x100.

Metabolic Assays

NAD+/NADH Assay: BMDM were plated in 96-well dishes at 50k cells/well. The next day, cells were treated with chemical compound or infected with *Salmonella typhimurium*. Plates were centrifuged at 500g for 5min at room temperature, after which culture medium was aspirated and 100 μL lysis buffer (Cayman Chemical) added to each well. Plates were nutated at room temperature for 30min and then centrifuged at 1000g for 10min at 4C. Supernatants were transferred to wells of a new plate, and 100 μL NAD+/NADH reaction solution (Cayman Chemical) was added to each well. After 1.5hr, A_{450} was measured.

650 *NADH Assay*: Cells were treated and lysates harvested as for the NAD+/NADH assay. After this,
651 NAD+ was decomposed by heating at 60˚C for 30min. Then, reaction solution was added and
652 after 1.5hr, A_{450} was measured.
653 *Lactate release assay:* BMDM were plated in 96-well dishes at 50k cells/well. The next day,
654 cells were treated with chemical compound or infected with *Salmonella typhimurium* in phenol
655 red-free DMEM. Plates were centrifuged at 500g for 5min at room temperature, after which 50
656 µL of supernatant/well was transferred to a new 96-well dish. Lactate reaction solution (50 µL;
657 Eton Biosciences) was added. After 30min, the reaction was quenched with 50 µL/well of 0.5M
658 acetic acid and A_{490} was measured.
659 *ATP assay:* BMDM were plated in opaque-walled 96-well dishes at 50k cells/well. The next day,
660 the cells were treated with chemical compounds in 100 µL well volume. After 1hr of treatment at
661 37C, the plate was brought to room temperature for 30min as per manufacturer's instructions
662 (Promega – CellTiter Glo). ATP reaction mixture was added directly to wells (100 µL/well) and
663 plate was nutated for 2 min to lyse cells. Plate was allowed to stabilize for 10-15min at room
664 temperature, after which luminescence was read by plate reader (1 sec integration time/well).
665
666 **Seahorse Analyzer Assay**
667 For ECAR measurements, BMDM were analyzed using a Seahorse XF96 Analyzer. On the day
668 prior to the assay $8x10^4$ BMDM were plated per well of a 96-well Seahorse Analyzer plate. The
669 next day, cells were washed with and then immersed in 180 mL Assay Medium (RPMI at pH 7.4
670 with 2 mM L-glutamine and without HEPES or sodium bicarbonate). Cells were incubated in a
671 CO_2-free incubator for 1hr at 37˚C. At initiation of assay, the plate was loaded into the Seahorse
672 Analyzer, allowed to equilibrate, and compounds injected in Assay Medium with fresh glucose.

ECAR was measured for 2hrs after compound injection. Cells were stained with Hoechst and counted after conclusion of assay. Measured ECAR values were normalized to cell number and averaged across each condition.

Fluorescent Glucose Assays

The fluorescent glucose analog 2-NBDG (Cayman Chemical; Abs/Em 465/540 nm) was used to monitor glucose uptake by both infected and uninfected BMDM. BMDM were infected with SL1344 *Salmonella typhimurium* grown to stationary phase at an MOI of 100:1. After 1hr, media was changed to DMEM with high gentamicin (100 μg/mL) to kill extracellular bacteria. After 1hr, BMDM were washed with plain DMEM and then incubated in DMEM with low gentamicin and 10 μM 2-NBDG. For microscopy analysis, cells were fixed and mounted in Vectashield with DAPI after 4hrs of infection. 2-NDBG was imaged using 'FITC' absorption/emission settings in ZenBlack software on a Zeiss LSM700 microscope. Quantification of average cytosolic 2-NBDG fluorescence was done using ImageJ software. In the uninfected condition, cytosol was identified as 2-NBDG (+) areas proximal to nuclei. In the infected condition, cytosol was identified as areas proximal to nuclei that were not *Salmonella typhimurium* (+). 4 fields per sample were quantified and the average and standard deviation of average cytosolic 2-NDBG fluorescence measurements reported. For measurement of 2-NBDG uptake into *S. typhimurium*, after 7hr of infection BMDM were lysed in 0.1% Triton-X-100 in PBS for 10min. Lysates were centrifuged at 5000g/10min/4˚C. Supernatant was aspirated and the resulting bacterial pellet resuspended in PBS, transferred to an opaque 96-well plate, and measured in triplicate on a plate reader at Abs/Em 465/540 nm.

***Salmonella* Replication Assays** *Salmonella typhimurium* (strain 12023) expressing a replication plasmid were grown overnight in LB containing 0.2% arabinose. BMDM were plated in 12-well dishes at 500k cells/well and infected with *Salmonella typhimurium* strain NCTC 12023 at MOI 25:1. At 12, 16, and 24 hours post-infection, BMDM were lysed and bacterial samples analyzed by flow cytometry. Generations of bacteria were calculated as previously described by Helaine et al. For *in vitro* growth curves, *S. typhimurium* were grown in MgM-MES minimal media supplemented with 2 mM glucose, 2 mM pyruvate, or vehicle (ddH_2O). OD_{600} was measured at various timepoints after inoculation of culture.

Mitochondrial ROS Measurement

BMDM were plate in 12-well dishes, primed for 3hr with 100 ng/mL LPS, and then stimulated in the presence or absence of pyruvate. BMDM were labeled for the last 15min of treatment with 2.5 μM MitoSOX Red (Life Technologies), collected, centrifuged for 5min at 2000rpm at 4˚C, then resuspending in ice cold PBS with 0.5% BSA and analyzed by flow cytometry (488 nm excitation, PE channel collection for MitoSOX Red). >25,000 cells were analyzed per condition.

K+ Efflux Experiments

LPS-primed BMDM were treated with NLRP3-activating compound in Ringer's buffer with varying concentrations of K+. Osmolarity was kept constant by varying NaCl concentration accordingly.

Synthetic Protocols:

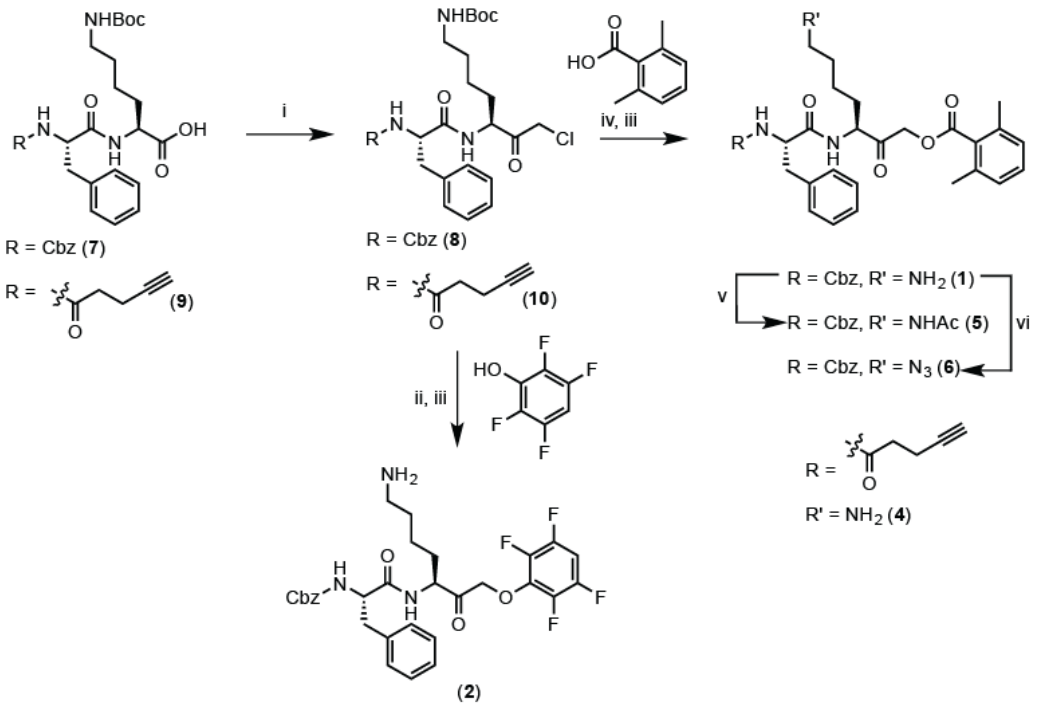

718

719 Reagents and conditions: i. IBCF, NMM, THF, -77°C, 1 hr, then CH_2N_2, -77°C, 1 hr, then warm
720 to RT, 3 hr, then 1:1 HCl:AcOH. ii. 2,3,5,6-tetrafluorophenol, KF, DMF, 80°C, 2 hr. iii. 50%
721 TFA in DCM, 30 min. iv. 2,6-dimethylbenzoic acid, KF, DMF, 9 hr. v. Acetyl chloride, TEA,
722 DCM, 30 min. vi. imidazole-1-sulfonyl azide, K_2CO_3, $CuSO_4$, MeOH, o/n.

723

724 *General procedure for chloromethylketone (CMK) synthesis:*

725 Peptide carboxylic acid (1eq), was stirred with isobutyl chloroformate (1.1 eq) and N-methyl
726 morpholine (1.2 eq) in anhydrous THF in a bath of dry ice/isopropanol for 1 hour, after which a
727 solution of CH_2N_2 (approximately 1.7 eq, freshly generated from diazald) was added. The
728 mixture was stirred in dry ice/isopropanol for 1 hour, and then brought to room temperature and
729 stirred for 3 hours. The reaction was quenched with 1:1 concentrated HCl:HOAc (v:v). Ethyl
730 acetate was added to the crude reaction mixture and the organic layer was washed with H_2O,

saturated $NaHCO_3$, and brine. The organic layers were pooled and dried with $MgSO_4$, and concentrated *in vacuo* to yield crude chloromethylketone.

General procedure for acyloxymethylketone (AOMK) synthesis:

Chloromethylketone (1 eq) was stirred with potassium fluoride (3 eq) in anhydrous DMF for 15 minutes. 2,6-dimethylbenzoic acid (1.1 eq) was added and the reaction mixture stirred for 9 hours at room temperature.

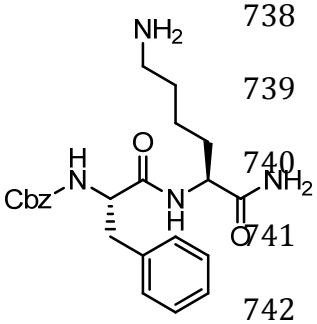

Synthesis of NR-GB111 (3)

Rink resin (1g, 0.59 mmol) was taken up in DMF and deprotected in 20% piperidine in DMF for 45 minutes at room temperature. The resin was washed with DMF. Fmoc-Lys(Boc)-OH (829 mg, 3 eq, 1.77 mmol), HOBt (239 mg, 3 eq, 1.77 mmol), and DIC (277 µL, 3 eq, 1.77 mmol) were added and the reaction mixture nutated for four hours. The resin was washed with DCM and DMF and the Fmoc group removed by incubation with 20% piperidine in DMF for 45 minutes. The resin was washed with DMF and Z-Phe-OH (530 mg, 3 eq, 1.77 mmol), HOBt (239 mg, 3eq, 1.77 mmol), and DIC (277 µL, 3 eq, 1.77 mmol) were added and the reaction mixture nutated overnight at room temperature. The resin was washed with DCM and DMF. The product NR-GB111 was cleaved from the Rink resin using 95% TFA, 2.5% triisopropylsilane, and 2.5% H_2O for 30 minutes. The crude was purified by HPLC (reverse phase C_{18} column, CH_3CN/H_2O 0.1% TFA, 5:95 to 80:20 over 9 column volumes (CVs) Pure fractions were lyophilized and 5.55 mg (0.013 mmol, 2.2% yield) **NR-GB111 (3)** were afforded as a white powder.

^{1}H NMR (500 MHz, CD_3OD) δ 7.36 – 7.19 (m, 10H), 5.03 (q, *J* = 12.6 Hz, 2H), 4.38 – 4.27 (m, 2H), 3.08 (dd, *J* = 13.7, 6.5 Hz, 1H), 2.92 (dd, *J* = 13.7, 8.6 Hz, 1H), 2.86 (t, *J* = 7.6 Hz, 2H), 1.93 – 1.79 (m, 1H), 1.69 – 1.53 (m, 3H), 1.47 – 1.32 (m, 2H).

HRMS (ES+): $[M+H+]^+$ calculated for $C_{23}H_{30}N_4O_4$ expected mass 427.2345 found 427.2345.

LCMS (ES+): retention time 5.57 minutes.

Synthesis of GB-IA (4)

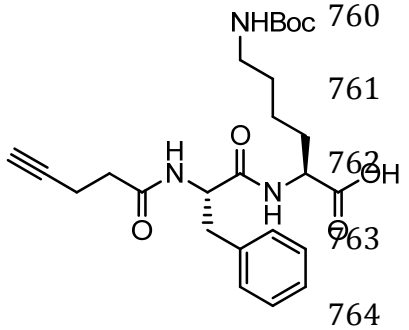

pent-4-ynamido-Phe-Lys(Boc)-OH (9)

Chlorotrityl resin (900 mg, 1.134 mmol, 1 eq) was swelled in anhydrous DCM. Fmoc-Lys(Boc)-OH (798 mg, 1.701 mmol, 1.5 eq) and DIPEA (402 µL, 2.31 mmol, 2 eq) were added and the reaction mixture nutated for 3 hours at room temperature. 500 µL anhydrous methanol was added for 30 minutes. The resin was washed with DCM, DMF, and then resin loading measured (0.531 mmol). The Fmoc group was removed by nutating the resin in 5% DEA in DMF for 30 minutes at room temperature. The resin was washed with DMF and Fmoc-Phe-OH (617 mg, 1.593 mmol, 3 eq), HOBt (215 mg, 1.593 mmol, 3 eq), and DIC (249 µL, 1.593 mmol, 3 eq) were added and the reaction mixture nutated for 2 hours at room temperature. The resin was washed with DCM and DMF and the Fmoc group removed by nutating in 5% DEA in DMF for 30 minutes. The resin was washed with DCM and DMF and 4-pentynoic acid (156 mg, 1.593 mmol, 3eq), HOBt (215 mg, 1.593 mmol, 3 eq), and DIC (249 µL, 1.593 mmol, 3 eq) were added and the reaction mixture nutated overnight at room temperature. Intermediate **9** was cleaved from resin using 1% TFA in DCM for 15 minutes. Concentration with toluene *in vacuo* yielded a white crystalline solid. The crude was purified by

HPLC (reverse phase C_{18} column, CH_3CN/H_2O 0.1% TFA, 10:90 to 80:20 over 9 CVs. Pure fractions were lyophilized and 160 mg (0.428 mmol, 80.6% yield) Intermediate **9** were afforded as a white powder.

pent-4-ynamido-Phe-Lys(Boc)-CMK (10)

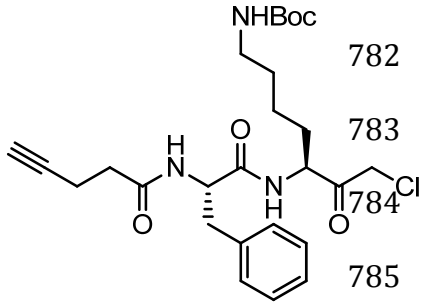

Carboxylic acid **9** (127 mg, 0.34 mmol was converted to the chloromethylketone using the procedure described above. The crude material was purified by flash column chromatography (20% ethyl acetate in hexane -> 60% ethyl acetate in hexane), and pure fractions pooled to yield 25.6 mg (0.06 mmol, 19% yield) of white crystalline solid.

GB-IA (4).

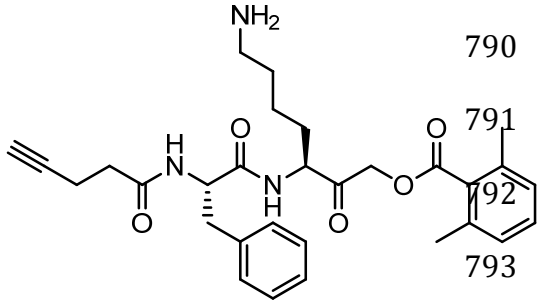

Intermediate **10** (25.6 mg, 0.05 mmol, 1 eq) was converted to the AOMK following the general procedure. The crude was purified by HPLC (reverse phase C_{18} column, CH_3CN/H_2O 0.1% TFA, 20:80 to 60:40 in x column volumes). Pure fractions were pooled and lyophilized. The lyophilized fractions were taken up in 50% TFA in DCM and stirred for 1 hour at room temperature. The reaction was concentrated with toluene *in vacuo* to yield 4.68 mg (9 μmol, 5.6% yield) of white crystalline solid, **GB-IA (4)**.

^{1}H NMR (400 MHz, $CD_3OD/CDCl_3$ 1/1) δ 7.32 – 7.24 (m, 4H), 7.23 – 7.15 (m, 2H), 7.06 – 7.01 (m, 2H), 4.61 – 4.41 (m, 4H), 3.10 (dd, *J* = 13.6, 8.4 Hz, 1H), 3.00 (dd, *J* = 13.6, 7.4 Hz, 1H),

2.89 (t, *J* = 7.4 Hz, 2H), 2.44 – 2.39 (m, 4H), 2.35 (s, 6H), 2.16 (t, *J* = 2.2 Hz, 1H), 2.01 – 1.84 (m, 1H), 1.72 – 1.53 (m, 3H), 1.51 – 1.34 (m, 2H).

HRMS (ES+): $[M+H+]^+$ calculated for $C_{30}H_{37}N_3O_5$ expected mass 520.2811 found 520.2797.

LCMS (ES+): retention time 6.55 minutes.

Synthesis of ac-GB111 (5), az-GB (6), and GB111-PMK (2)

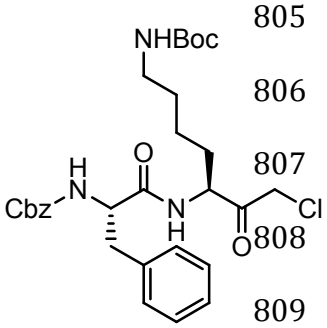

Cbz-Phe-Lys(Boc)-CMK (8). Intermediate **7** (200 mg, 0.38 mmol, 1 eq) was converted to the chloromethyl ketone as described in the general procedure above. The crude was purified by flash column chromatography (20% ethyl acetate in hexane -> 60% ethyl acetate in hexane), and pure fractions pooled to yield 150 mg (0.27 mmol, 70% yield) of white crystalline solid.

GB111-NH_2 (1). Intermediate **8** (30 mg, 0.05 mmol) was converted to the acyloxymethylketone as described above in the general procedure. The crude was purified by HPLC (reverse phase C_{18} column, CH_3CN/H_2O 0.1% TFA, 20:80 to 60:40 over 25 minutes, 15 mL per minute. Pure fractions were lyophilized. Lyophilized fractions were taken up in 50% TFA in DCM and stirred for 30 minutes, after which the reaction mixture was concentrated with toluene *in vacuo* to yield 14.5 mg (25.26 μmol, 51%) **GB111-NH_2** as a white powder. Refer to Patent US2007/36725 A1 for previous synthetic scheme of Intermediates **7** and **8** and GB111-NH_2 and compound characterization.

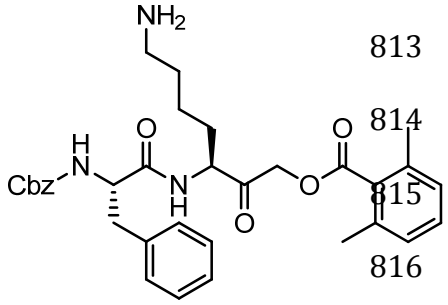

ac-GB111 (5). GB111-NH_2 (**1**) (4.58 mg, 8.81 □mol,1 eq) was dissolved in anhydrous DCM.

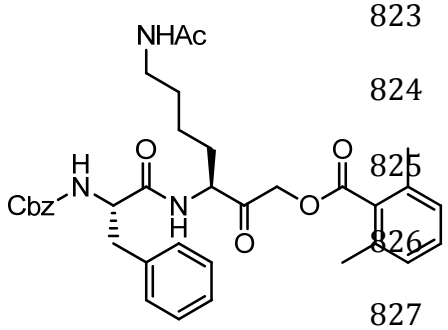

Triethylamine (1.35 □L, 9.69 □mol, 1.1 eq) was added and the reaction mixture stirred for 5 minutes before the addition of acetyl chloride (0.94 µL, 13.21 µmol, 1.5 eq). The mixture was stirred at room temperature for 30 minutes and then concentrated *in vacuo*. The crude was taken up in DMSO and purified by HPLC (reverse phase C_{18} column, CH_3CN/H_2O 0.1% TFA, 20:80 to 50:50 over column volumes. Pure fractions were lyophilized to yield 0.45 mg (0.73 µmol, 8.2% yield) of white crystalline solid, **ac-GB111 (5)**.

^{1}H NMR (400 MHz, $CD_3OD/CDCl_3$ 1/1) δ 7.33 – 7.10 (m, 11H), 6.99 (d, *J* = 7.4 Hz, 2H), 5.00 – 4.98 (m, 2H), 4.65 (s, 2H), 4.42 (dd, *J* = 11.3, 6.3 Hz, 2H), 3.17 – 3.09 (m, 1H), 3.09 – 3.00 (m, 2H), 2.97 – 2.88 (m, 1H), 2.32 (s, 6H), 1.86 (s, 3H), 1.62 – 1.51 (m, 1H), 1.44 – 1.34 (m, *3*H), 1.31 – 1.22 (m, 2H).

HRMS (ES+): $[M+H+]^+$ calculated for $C_{35}H_{41}N_3O_7$ expected mass 616.3023 found 616.3017.

LCMS (ES+): retention time 8.08 minutes.

az-GB (6). GB111-NH_2 (**1**) (2.2 mg, 3.83 □mol, 1 eq) was dissolved in anhydrous methanol.

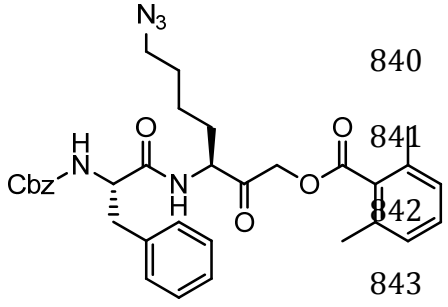

K_2CO_3 (1.68 mg, 12.2 µmol, 3 eq), imidazole-1-sulfonyl azide HCl[53] (0.9 mg, 5.2 µmol, 1.36 eq), and Cu(II)SO_4 pentahydrate (0.0034 mg, 0.014 mmol, 0.003 eq) were added and the reaction mixture was stirred overnight at room temperature. The reaction mixture was concentrated *in vacuo*. The crude was taken up in DMSO and purified by HPLC (reverse phase C_{18} column,

CH_3CN/H_2O 0.1% TFA, 20:80 to 60:40 over column volumes. Pure fractions were lyophilized to yield 1.77 mg (2.95 μmol, 77% yield) of white crystalline solid, **az-GB (6)**.

^1H NMR (500 MHz, $CD_3OD/CDCl_3$ 1/1) δ 7.37 – 7.19 (m, 11H), 7.06 (d, *J* = 7.6 Hz, 2H), 5.08 (s, 2H), 4.71 – 4.60 (m, 2H), 4.51 – 4.44 (m, 2H), 3.25 (t, *J* = 6.8 Hz, 2H), 3.11 (dd, *J* = 13.6, 7.5 Hz, 1H), 2.99 (dd, *J* = 13.6, 7.4 Hz, 1H), 2.39 (s, *J* = 6.3 Hz, 6H), 1.99 – 1.87 (m, 1H), 1.68 – 1.51 (m, 3H), 1.51 – 1.32 (m, 2H).

HRMS (ES+): $[M+H+]^+$ calculated for $C_{33}H_{37}N_5O_6$ expected mass 600.2822 found 600.2818.

LCMS (ES+): retention time 8.90 minutes.

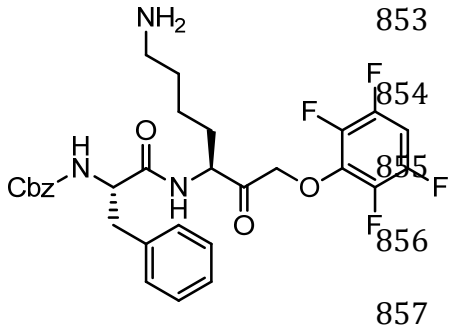

GB111-PMK (2). Potassium fluoride (15.56 mg, 0.27 mmol, 3 eq) and 2,3,5,6-tetrafluorophenol (16.3 mg, 0.1 mmol, 1.1 eq) were added to DMF and the reaction mixture stirred at 80C for 10 minutes. Intermediate **10** (50.41 mg, 0.09 mmol, 1 eq) was taken up in DMF and added to the reaction mixture. This mixture was stirred for 2 hours at 80C then concentrated *in vacuo*. The crude was taken up in DCM and purified by flash column chromatography (hexane -> 55% ethyl acetate in hexane). Pure fractions were pooled and concentrated *in vacuo*. This product was taken up in 50% TFA in DCM and stirred for 30 minutes, after which it was concentrated with toluene *in vacuo* to yield 35.3 mg **GB111-PMK (2)** (0.06 mmol, 65% yield) as a white crystalline solid.

^1H NMR (500 MHz, cd_3od) δ 7.35 – 7.19 (m, 10H), 7.16 – 7.06 (m, *J* = 14.4, 8.7, 5.3 Hz, 1H), 5.09 – 4.94 (m, 2H), 4.81 – 4.68 (m, 2H), 4.55 – 4.44 (m, 1H), 4.39 – 4.32 (m, 1H), 3.09 – 2.91 (m, 2H), 2.85 (t, *J* = 7.6 Hz, 2H), 1.95 – 1.74 (m, *J* = 40.2 Hz, 1H), 1.68 – 1.49 (m, 3H), 1.48 – 1.34 (m, 2H).

HRMS (ES+): $[M+H+]^+$ calculated for $C_{30}H_{31}F_4N_3O_5$ expected mass 590.2278 found 590.2278.

LCMS (ES+): retention time 7.04 minutes.

Acknowledgments

We thank the Bogyo lab for helpful discussions regarding the direction of this project, M. Child and S. Ewald for comments on the manuscript, M. Spitzer for comments and flow cytometry assistance, A. Ondrus, T.-H. Lee, A. Bhaduri, and E. LaGory for assay advice and reagents. This work was supported by the National Science Foundation under grant DGE-114747 (to L.E.S.) and by the National Institutes of Health under grants R01 EB005011 and R01 CA179253 (to M.B.) and AI063302 and AI065359 (to D.M.M.). E.W. is grateful for financial support from the Smith Family Foundation, the Damon Runyon Cancer Research Foundation (DRR-18-12) and Boston College.

Author Contributions

L.E.S., N.E., T.N., D.M.M, E.W., and M.B. designed the experiments. L.E.S., Y.Q., N.E., and W.L. performed the experiments. All authors analyzed the data. L.E.S. and M.B. wrote the manuscript.

Competing Financial Interests

The authors declare no competing financial interests.

Ethics Statement

This work was approved under ABP protocol 1331 (Entitled Chemical probes to study host responses to bacterial pathogens) and APLAC protocol 18026. Primary cells were isolated from mouse bone marrow following strict accordance with the NIH guide for the care and use of laboratory animals. These protocols were reviewed and approved by the Environmental Health

and Safety Department of Stanford University and the Institutional Animal Care and Use Committee of Stanford University, respectively.

Additional Information

Correspondence and requests for materials should be sent to M.B.

References

1. Medzhitov, R. Origin and physiological roles of inflammation. *Nature* **454,** 428–435 (2008).
2. Lamkanfi, M. & Dixit, V. M. Mechanisms and Functions of Inflammasomes. *Cell* **157,** 1013–1022 (2014).
3. Fink, S. L. & Cookson, B. T. Caspase-1-dependent pore formation during pyroptosis leads to osmotic lysis of infected host macrophages. *Cell Microbiol* **8,** 1812–1825 (2006).
4. Ben A Croker, O'Donnell, J. A. & Gerlic, M. Pyroptotic death storms and cytopenia. *Current Opinion in Immunology* **26,** 128–137 (2014).
5. Fernandes-Alnemri, T., Yu, J.-W., Datta, P., Wu, J. & Alnemri, E. S. AIM2 activates the inflammasome and cell death in response to cytoplasmic DNA. *Nature* **458,** 509–513 (2009).
6. Hornung, V. *et al.* AIM2 recognizes cytosolic dsDNA and forms a caspase-1-activating inflammasome with ASC. *Nature* **458,** 514–518 (2009).
7. Burckstummer, T. *et al.* An orthogonal proteomic-genomic screen identifies AIM2 as a cytoplasmic DNA sensor for the inflammasome. *Nature Immunology* **10,** 266–272 (2009).
8. Jones, J. W. *et al.* Absent in melanoma 2 is required for innate immune recognition of Francisella tularensis. *Proceedings of the National Academy of Sciences* **107,** 9771–9776

914 9. Sutterwala, F. S., Haasken, S. & Cassel, S. L. Mechanism of NLRP3 inflammasome
915 activation. *Annals of the New York Academy of Sciences* **1319,** 82–95 (2014).
916 10. Storek, K. M. & Monack, D. M. Bacterial recognition pathways that lead to
917 inflammasome activation. *Immunological Reviews* **265,** 112–129 (2015).
918 11. Broz, P. *et al.* Redundant roles for inflammasome receptors NLRP3 and NLRC4 in host
919 defense against Salmonella. *Journal of Experimental Medicine* **207,** 1745–1755 (2010).
920 12. Blum, G. *et al.* Dynamic imaging of protease activity with fluorescently quenched
921 activity-based probes. *Nature Chemical Biology* **1,** 203–209 (2005).
922 13. Verdoes, M. *et al.* A Nonpeptidic Cathepsin S Activity-Based Probe for Noninvasive
923 Optical Imagingof Tumor-Associated Macrophages. *Chem. Biol.* **19,** 619–628 (2012).
924 14. Puri, A. W., Broz, P., Shen, A., Monack, D. M. & Bogyo, M. Caspase-1 activity is
925 required to bypass macrophage apoptosis upon Salmonella infection. *Nature Chemical*
926 *Biology* **8,** 745–747 (2012).
927 15. Weerapana, E., Speers, A. E. & Cravatt, B. F. Tandem orthogonal proteolysis-activity-
928 based protein profiling (TOP-ABPP)—a general method for mapping sites of probe
929 modification in proteomes. *Nat Protoc* **2,** 1414–1425 (2007).
930 16. Miyadera, H. *et al*. Atpenins, potent and specific inhibitors of mitochondrial complex II
931 (succinate-ubiquinone oxidoreductase). *Proceedings of the National Academy of Sciences*
932 **100,** 473–477 (2003).
933 17. Street, J. C., Alfieri, A. A. & Koutcher, J. A. Quantitation of Metabolic and
934 Radiobiological Effects of 6-Aminonicotinamide inRIF-1 Tumor Cells in Vitro'. *Clinical*
935 *Cancer Research* **57,** 3956–3962 (1997).
936 18. Endo, A., Hasumi, K., Sakai, K. & Kanbe, T. Specific Inhibition of Glyceraldehyde-3-

phosphate dehydrogenase by koningic acid (heptelidic acid). *The Journal of Antibiotics* **38,** 920–925 (1985).

19. Jung, D.-W. *et al.* A Unique Small Molecule Inhibitor of Enolase Clarifies Its Role in Fundamental Biological Processes. *ACS Chem. Biol.* **8,** 1271–1282 (2013).

20. Ekkebus, R. *et al.* On Terminal Alkynes That Can React with Active-Site Cysteine Nucleophiles in Proteases. *J. Am. Chem. Soc.* **135,** 2867–2870 (2013).

21. Weerapana, E. *et al.* Quantitative reactivity profiling predicts functional cysteines in proteomes. *Nature* **468,** 790–795 (2010).

22. Kato, M., Sakai, K. & Endo, A. Koningic acid (heptelidic acid) inhibition of glyceraldehyde-3-phosphate dehydrogenases from various sources. *Biochimica et Biophysica Acta* **1120,** 113–116 (1992).

23. Ishii, T. & Uchida, K. Induction of reversible cysteine-targeted protein oxidation by an endogenous electrophile 15-deoxy-delta12,14-prostaglandin J2. *Chem. Res. Toxicol.* **17,** 1313–1322 (2004).

24. Singh, J., Petter, R. C., Baillie, T. A. & Whitty, A. The resurgence of covalent drugs. *Nat Rev Drug Discov* **10,** 307–317 (2011).

25. Pietzke, M., Zasada, C., Mudrich, S. & Kempa, S. Decoding the dynamics of cellular metabolism and the action of 3-bromopyruvate and 2-deoxyglucose using pulsed stable isotope-resolved metabolomics. *Cancer Metab* **2,** 1–11 (2014).

26. Krawczyk, C. M. *et al.* Toll-like receptor-induced changes in glycolytic metabolism regulate dendritic cell activation. *Blood* **115,** 4742–4749 (2010).

27. Shestov, A. A. *et al.* Quantitative determinants of aerobic glycolysis identify flux through the enzyme GAPDH as a limiting step. *eLife* **3,** (2014).

28. Tavakoli, S., Zamora, D., Ullevig, S. & Asmis, R. Bioenergetic Profiles Diverge During Macrophage Polarization: Implications for the Interpretation of 18F-FDG PET Imaging of Atherosclerosis. *Journal of Nuclear Medicine* **54,** 1661–1667 (2013).

29. Tannahill, G. M. *et al.* Succinate is an inflammatory signal that induces IL-1β through HIF-1α. *Nature* **496,** 238–242 (2013).

30. Tschopp, J. & Schroder, K. NLRP3 inflammasome activation: the convergence of multiple signalling pathways on ROS production? *Nature Reviews Immunology* **10,** 210–215 (2010).

31. Muñoz-Planillo, R. *et al.* K+ Efflux Is the Common Trigger of NLRP3 Inflammasome Activation by Bacterial Toxins and Particulate Matter. *Immunity* **38,** 1142–1153 (2013).

32. Bowden, S. D., Rowley, G., Hinton, J. C. D. & Thompson, A. Glucose and Glycolysis Are Required for the Successful Infection of Macrophages and Mice by Salmonella enterica Serovar Typhimurium. *Infection and Immunity* **77,** 3117–3126 (2009).

33. Bowden, S. D. *et al.* Nutritional and Metabolic Requirements for the Infection of HeLa Cells by Salmonella enterica Serovar Typhimurium. *PLoS ONE* **9,** e96266 (2014).

34. Zhao, Y. *et al.* The NLRC4 inflammasome receptors for bacterial flagellin and type III secretion apparatus. *Nature* **477,** 596–600 (2011).

35. Broz, P. *et al.* Caspase-11 increases susceptibility to Salmonella infection in the absence of caspase-1. *Nature* **490**, 288-292 (2012).

36. Helaine, S. *et al.* Dynamics of intracellular bacterial replication at the single cell level. *Proceedings of the National Academy of Sciences* **107,** 3746–3751 (2010).

37. Biswas, S. K. & Mantovani, A. Orchestration of Metabolism by Macrophages. *Cell Metabolism* **15,** 432–437 (2012).

983 38. Kuemmerle-Deschner, J. B. *et al.* NLRP3 E311K mutation in a large family with Muckle-
984 Wells syndrome - description of a heterogeneous phenotype and response to treatment.
985 *Arthritis Research & Therapy* **13,** R196 (2011).
986 39. Wen, H., Ting, J. P.-Y. & O'Neill, L. A. J. A role for the NLRP3 inflammasome in
987 metabolic diseases—did Warburg miss inflammation? *Nature Immunology* **13,** 352–357
988 (2012).
989 40. Wen, H. *et al.* Fatty acid–induced NLRP3-ASC inflammasome activation interferes with
990 insulin signaling. *Nature Immunology* **12,** 408–415 (2011).
991 41. Ganapathy-Kanniappan, S. & Geschwind, J.-F. H. Tumor glycolysis as a target for cancer
992 therapy: progress and prospects. *Molecular Cancer* **12,** 1–11 (2013).
993 42. Zhou, R., Yazdi, A. S., Menu, P. & Tschopp, J. A role for mitochondria in NLRP3
994 inflammasome activation. *Nature* **211,** 653–668 (2010).
995 43. Wynosky-Dolfi, M. A. *et al.* Oxidative metabolism enables Salmonella evasion of the
996 NLRP3 inflammasome. *Journal of Experimental Medicine* **211,** 653–668 (2014).
997 44. Eisele, N. A. *et al.* Salmonella Require the Fatty Acid Regulator PPARδ for the
998 Establishment of a Metabolic Environment Essential for Long-Term Persistence. *Cell*
999 *Host and Microbe* **14,** 171–182 (2013).
1000 45. Blatnik, M., Frizzell, N., Thorpe, S. R. & Baynes, J. W. Inactivation of Glyceraldehyde-3-
1001 Phosphate Dehydrogenase by Fumarate in Diabetes: Formation of S-(2-Succinyl)Cysteine,
1002 a Novel Chemical Modification of Protein and Possible Biomarker of Mitochondrial
1003 Stress. *Diabetes* **57,** 41–49 (2007).
1004 46. Chawla, A., Nguyen, K. D. & Goh, Y. P. S. Macrophage-mediated inflammation in
1005 metabolic disease. *Nature Reviews Immunology* **11,** 738–749 (2011).

47. Young, P., Cawthorne, M. A., Levy, A. L. & Wilson, K. Reduced maximum capacity of glycolysis in brown adipose tissue of genetically obese, diabetic (db/db) mice and its restoration following treatment with a thermogenic B-adrenoceptor agonist. *FEBS Journal* **176,** 16–20 (1984).

48. Strowig, T., Henao-Mejia, J., Elinav, E. & Flavell, R. Inflammasomes in health and disease. *Nature* **481,** 278–286 (2012).

49. Kayagaki, N. *et al.* Non-canonical inflammasome activation targets caspase-11. *Nature* **479,** 117–121 (2011).

50. Mariathasan, S. *et al.* Differential activation of the inflammasome by caspase-1 adaptors ASC and Ipaf. *Nature* **430,** 213–218 (2004).

51. Chandler, C. S. & Ballard, F. J. Distribution and degradation of biotin-containing carboxylases in human cell lines. *Biochemical Journal* **232,** 385–393 (1985).

52. Child, M. A. *et al.* small-molecule inhibition of a depalmitoylase enhances Toxoplasma host-cell invasion. *Nature Chemical Biology* **9,** 651–656 (2013).

53. Goddard-Borger, E. D. & Stick, R. V. An Efficient, Inexpensive, and Shelf-Stable Diazotransfer Reagent: Imidazole-1-sulfonyl Azide Hydrochloride. *Org. Lett.* **9,** 3797–3800 (2007).

Figure Legends

Figure 1. Identification of the NLRP3 inflammasome activator GB111-NH_2. (**A**) Structure of GB111-NH_2. (**B**) Western blot and activity-based probe analysis of caspase-1 activation. BMDM primed with 100 ng/mL LPS for 3 hours were then treated with GB111-NH_2. Intact cells were labeled with the caspase-1 probe AWP28 (1 μM) for the last hour before lysate harvest. Whole cell lysates were separated by SDS-PAGE. AWP28 labeling was analyzed by fluorescence scan and caspase-1 processing analyzed by western blot. Gray arrowheads indicate active forms of caspase-1 labeled by AWP28. HSP90 serves as loading control. (**C**) LPS-primed BMDM were treated with the indicated concentrations of GB111-NH_2 for 2 hours. Supernatants were analyzed by ELISA. (**D**) LPS-primed BMDM were treated with 10 μM GB111-NH_2 for 2 hours, labeled with AWP28, fixed, stained for ASC and DAPI, and visualized by confocal microscopy. Scale bar 10 μm. (**E-F**) BMDM of the indicated genetic backgrounds were treated with GB111-NH_2 as in (**D**) and inflammasome foci/nuclei quantified. At least 4 fields of view (20x objective, 0.5x zoom) were taken per condition per experiment, ~2000 cells/condition. (**G**) LPS-primed BMDM were treated with the indicated compounds (ATP: 5 mM; nigericin: 10 μM; GB111-NH_2: 10 μM) and supernatant analyzed by ELISA. (**H**) BMDM of the indicated genetic backgrounds werere treated as in (**D**) and supernatant analyzed by ELISA. (**I**) BMDM were primed with LPS or vehicle, then treated with GB111-NH_2 for 2 hours. Whole cell lysates were separated by SDS-PAGE, blotted for pro-IL-1β, stripped, and reblotted for HSP90. (**J**) Cell death in LPS-primed, GB111-NH_2-treated BMDM was analyzed by LDH release. (**K**) LPS-primed BMDM were treated with 10 μM GB111-NH_2 for 2hr, labeled with AWP28, stained for Annexin V (AnnV) and propidium iodide (PI), and visualized by microscopy. White arrowhead indicates AWP28 focus. Scale bar 10 μm. In all cases, data are representative of at least n=3 experiments and error

bars indicate mean +/- sd of technical triplicate. Statistical significance was analyzed using an unpaired, two-tailed t test.

Figure 1 – figure supplement 1. Secreted IL-1β is the bioactive, p17 form. Supernatant from BMDM treated with the indicated concentrations of GB111-NH_2 were analyzed by western blot for IL-1β. Different processing variants are indicated.

Figure 1 – figure supplement 2. GB111-NH_2 does not impair secretion of TNF-α and dose-dependently reduces IL-6 secretion. LPS-primed BMDM were treated with the indicated concentrations of GB111-NH_2 for 2 hours and then analyzed for IL-6 (*left*) and TNF-α (*right*) production by ELISA.

Figure 2. Structure-activity relationship study and identification of GB111-NH_2 targets. (**A**) Structures of GB111-NH_2 analogs with structural changes highlighted in gray. LPS-primed BMDM were treated with analogs and supernatant IL-1β measured by ELISA. A dose response is shown above each analog. (**B**) Set-up of MudPIT target identification experiment. In all cases, data are representative of n=3 experiments. Error bars indicate mean +/- sd of technical triplicate.

Figure 2 – figure supplement 1. Az-GB is a functional probe version of GB111-NH_2. (**A**) BMDM were treated with GB111-NH_2 or az-GB and labeled with AWP28. Whole cell lysates were separated by SDS-PAGE and analyzed by fluorescence scan and western blotting. Gray arrowheads indicate active caspase-1 species. HSP90 serves as loading control. (**B**) SV40-immortalized macrophages were treated with az-GB. Lysates were reacted with TAMRA-alkyne under Click reaction conditions, separated by SDS-PAGE, and analyzed by fluorescence gel scan.

Figure 3. The phenotypically relevant targets of GB111-NH_2 are glycolytic enzymes. (**A**) LPS-primed BMDM were treated with the indicated compounds (GAPDH inhibitor koningic acid = KA; 10 μM, α-enolase inhibitor ENOblock = EB; 20 μM, succinate dehydrogenase inhibitor Atpenin A5 = AA5; 10 μM, 6-phosphogluconate dehydrogenase inhibitor 6-aminonicotinamide = 6-AN; 500 μM) and IL-1β secretion was analyzed by ELISA. Whole cell lysates were separated by SDS-PAGE and blotted for pro-IL-1β. (**B**) BMDMs were treated with KA and EB and cell lysates were analyzed for caspase-1 processing by western blot. HSP90 serves as loading control. (**C**) BMDM were treated as in (**B**), labeled with AWP28, fixed, stained for ASC and DAPI, and analyzed by fluorescence microscopy. Scale bar 10 μm. (**D**) LPS-primed BMDM from the indicated genetic backgrounds were treated with KA or EB for 3 hours, fixed, stained for ASC and DAPI, and analyzed by confocal microscopy. At least 4 fields of view were captured per condition, ~2000 cells/condition/experiment. (**E**) LPS-primed BMDM of the indicated genetic backgrounds were treated with the indicated compounds (GB111-NH_2 – 10 μM for 2 hours, KA – 5 μM for 3 hours, EB – 20 μM for 3 hours, nigericin – 12.5 μM for 1 hour) and supernatant analyzed for IL-1β production by ELISA. (**F**) BMDM were treated as in (**B**). Whole cell lysates were separated by SDS-PAGE and blotted for pro-IL-1β, NLRP3, and α-tubulin.

Figure 3 – figure supplement 1. Cathepsin inhibition does not induce caspase-1 activation. BMDM were treated with GB111-NH_2 or structurally dissimilar cathepsin inhibitors CA074Me, E64d, and leupeptin. Caspase-1 activation was assessed by AWP28 labeling and cathepsin inhibition by BMV109 labeling. HSP90 serves as loading control.

Figure 3 – figure supplement 2. Koningic acid and ENOblock induce dose-dependent IL-1β secretion. LPS-primed BMDM were treated with the indicated concentrations of koningic acid or ENOblock for 3 hours and supernatants analyzed by ELISA.

Figure 4. Compounds covalently bind to reactive cysteines on GAPDH and α-enolase and inhibit enzyme activity *in vitro*. (**A**) Recombinant human GAPDH was pretreated with GB111-NH_2 and its analogs at the indicated concentrations for 1 hour in 0.1 M Tris-HCl pH 8.0, then labeled with az-GB (50 μM) for 1 hour. Mixtures were reacted with TAMRA-alkyne, separated by SDS-PAGE, and analyzed by fluorescence scan. Gels were silver stained to assess loading. % competition was calculated as 100-(fluor. $intensity_{cmpd+az\text{-}GB}$/fluor. $intensity_{az\text{-}GB\text{-}only}$). (**B**) Recombinant human α-enolase was labeled as described for GAPDH in (**A**). (**C**) GAPDH was incubated with NEM (5 μM), GB111-NH_2 (10 μM) or vehicle for 30 minutes, then labeled with iodoacetamide fluorescein (IAF; 10 μM) for 30 minutes. Reaction mixtures were separated by SDS-PAGE. Gels were analyzed by fluorescent scan and blotted for GAPDH to assess loading. (**D**) α-enolase was treated as described for GAPDH in (**E**) and blotted for α-enolase to assess loading. (**E**) Recombinant GAPDH and α-enolase were pretreated with inhibitors for 30 minutes and then enzyme activity assessed using substrate turnover assays. (**F**) GAPDH and α-enolase were incubated with GB111-NH_2 for the indicated amounts of time and then enzyme activity assessed. Data are representative of at least n=3 experiments and error bars indicate mean +/- sd of technical triplicate.

Figure 4 – figure supplement 1. az-GB binds to reactive cysteines on recombinant GAPDH and α-enolase in a manner that is dependent on enzyme activity. Recombinant human

GAPDH or α-enolase (rhGAPDH, rhEno1) were pretreated with vehicle (veh), N-ethylmaleimide (NEM, 5 μM), active (GB111-NH_2, 10 μM) or inactive (GB-IA, 50 μM) analogs, KA (5 μM) or EB (20 μM) for 30 minutes in PBS with 1% NP-40 and 0.1% SDS and then labeled with az-GB (50 μM). Reaction mixtures were reacted with TAMRA-alkyne, separated by SDS-PAGE, and analyzed by fluorescence scan and Coomassie Blue to assess loading. Black arrowhead indicates faster migrating active GAPDH species.

Figure 5. Inhibition of glycolytic flux creates a unique metabolic defect that activates the NLRP3 inflammasome. (**A**) Map of relevant metabolic pathways. (**B**) BMDM were stimulated with LPS or vehicle for 3 hours and then the indicated compounds for 2 hours, after which cytosolic NAD+/NADH ratio was measured. (**C**) BMDM were treated as in (**B**) and supernatants were analyzed for lactate production. Inhibitor concentrations are those from **Figure 3a**. (**D**) LPS-primed BMDM were stimulated with the indicated compounds for 2 hours and cytosolic NAD+/NADH was measured. (**E**) BMDM were treated as in (**B**) and cytosolic ATP concentration analyzed by ATP-coupled luminescence assay. (**F**) ECAR was measured in BMDM upon addition of fresh glucose-containing medium. Fresh medium contained vehicle (DMSO; gray squares) or 10 μM GB111-NH_2 -/+ 1 mM pyruvate (black/gray squares). Error bars represent mean +/- sd of 6 technical replicates per condition.

Figure 5 – figure supplement 1. A dose of nigericin that induces cell death with similar kinetics to GB111-NH_2 does not effect NADH production. LPS-primed BMDM were treated with nigericin (1 μM) or GB111-NH_2 (10 μM) for the indicated amounts of time (**A**) % LDH release was measured to assess the extent of cell death. (**B**) NADH production was measured in

cell lysates. Error bars are mean +/- sd of technical triplicate. Statistical difference between conditions was assessed using an unpaired, two–tailed t test.

Figure 5 – figure supplement 2. 2DG does not dramatically impair glycolytic flux or induce inflammasome formation. (**A**) Lactate production from 2-deoxyglucose (2DG at 10 mM) – treated LPS-primed BMDM was measured. (**B**) BMDM were treated as in (**A**) and analyzed for cytosolic NAD+/NADH. (**C**) LPS-primed BMDM were treated with GB111-NH_2 (10 μM) or 2DG (10 mM) for 2 hours and labeled with AWP28. BMDM were then fixed, stained for ASC and with DAPI, and inflammasome foci were quantified.

Figure 6. Addition of metabolites downstream of glycolysis prevents NLRP3 inflammasome activation induced by glycolytic disruption. (**A**) LPS-primed BMDM were treated with GB111-NH_2 for 2 hours in the presence of pyruvate (pyr; 1 mM) or cell-permeable esters of lactate (lac; 1 mM) and succinate (succ; 10 mM). Cells were fixed, stained for ASC and DAPI, and inflammasome foci/nuclei quantified. At least four fields of view were quantified per condition per experiment, ~2000 cells/condition. Error bars represent mean +/- sd of fields of view analyzed. (**B**) BMDM were primed with LPS and then treated with 10 μM GB111-NH_2 for 2 hours in the presence of the indicated concentrations of L-glutamine or succinate. Cells were fixed, stained for ASC and DAPI, and quantified by microscopy. Four fields of view (~2000 cells) were analyzed per condition. Error bars represent mean +/- sd of separate fields of view. (**C**) LPS-primed BMDM were treated with the indicated compounds in the presence or absence of pyruvate and analyzed as in (**A**). (**D**) BMDM were treated as in (**C**) and supernatants were analyzed for IL-1β by ELISA. (**E**) BMDM were treated as in (**C**) and cell death was measured by LDH release. (**F**) BMDM were treated with the indicated inhibitors, stained for ASC and DAPI, and quantified by microscopy as in (**B**). (**G**) BMDM were treated with GB111-NH_2 for 2 hours

in the presence or absence of pyruvate (1 mM), after which cytosolic NAD+/NADH was measured. (**H**) BMDM were treated as in (**i**) and cytosolic ATP measured by ATP-coupled luminescence assay. For ELISA and LDH release data, error bars represent mean +/- sd of technical triplicate. Data were analyzed for statistical significance using an unpaired, two-tailed t test.

Figure 7. NAD+/NADH ratio elevation and mitochondrial ROS accumulation are signals for NLRP3 inflammasome formation downstream of glycolytic disruption. (**A**) LPS-primed BMDM were treated with the indicated compounds (GB111-NH_2 - 10 μM, sodium pyruvate - 1 mM, AA5 - 10 μM, oligomycin A - 1 μM, rotenone - 5 μM) for 2 hours, after which cells were fixed, stained for ASC and DAPI, and visualized by microscopy. (**B**) Cells were treated as in (**A**) and cytosolic NAD+/NADH measured. (**C**) Cells were treated as in (**A**) and cytosolic ATP measured by ATP-coupled luminescence assay. (**D**) % Cells with ASC foci values from (**A**) are plotted against NAD+/NADH values from (**B**). Error bars are representative of mean +/- sd of technical triplicate from (**A**) and (**B**). (**E**) LPS-primed BMDM were treated with vehicle or 10 μM GB111-NH_2 in the presence or absence of 5 μM rotenone for 2 hours. Cells were fixed, stained for ASC and DAPI, and analyzed by microscopy. Four fields of view were collected per condition (~2000 cells). (**F**) Cells were treated as in (**E**) and cytosolic NAD+/NADH analyzed. Error bars represent mean +/- sd of technical triplicate. (**G**) BMDM were treated with 10 μM GB111-NH_2 or vehicle in the presence or absence of 1 mM pyruvate (pyr) and stained with MitoSOX (2.5 μM). Cells were analyzed for MitoSOX uptake by flow cytometry. (**H**) LPS-primed BMDMs were treated with GB111-NH_2 in the presence or absence of 4-hydroxyTEMPO (4-HT). Whole cell lysates and cell supernatants (sup) were separated by SDS-PAGE and

analyzed by western blot to detect the active p10 form of caspase-1. HSP90 serves as loading control. (**I**) BMDM were treated with nigericin (12.5 μM) or GB111-NH_2 (10 μM) in Ringer's buffer with increasing concentrations of K+. Cells were fixed, stained for ASC and DAPI, and inflammasome foci/nuclei quantified.

Figure 7 – figure supplement 1. ATP concentration does not correlate with inflammasome numbers. ATP concentration values from Figure 7A were plotted against % Cells with ASC foci from Figure 7B.

Figure 7 – figure supplement 2. K+ efflux is not required for GB111-NH_2 induced pyroptotic cell death. BMDM were treated with nigericin (12.5 μM) or GB111-NH_2 (10 μM) in Ringer's buffer with increasing concentrations of K+. After 3 hours, cell death was assessed by measuring % LDH release. Error bars are mean +/- sd of technical triplicate.

Figure 8. *Salmonella typhimurium* disrupts host cell glycolysis. (**A**) BMDMs were infected with *S. typhimurium* strain SL1344 grown to stationary phase and infected at the indicated multiplicity of infection (MOI; 25:1 and 100:1). At the indicated timepoints, cells were fixed and stained for ASC and DAPI. Inflammasome foci/nuclei were quantified. (**B**) BMDM were infected with ΔorgA (SPI-1 deficient) *S. typhimurium* grown to stationary phase. Cells were fixed at the indicated timepoints, stained for ASC and DAPI, and foci/nuclei quantified. (**C**) Cells were treated with the indicated compounds or infected with *S. typhimurium* grown to stationary phase (100:1 MOI) or log phase (10:1 MOI). Cells were fixed, stained for ASC, and ASC foci/nuclei were quantified. (**D**) BMDM were infected with 100:1 MOI stationary phase *S. typhimurium* for 5 hours. 2-NBDG (10 μM) or vehicle was added to media 2 hours post-infection.

Cells were washed, lysed, intracellular bacteria sedimented from whole cell lysate via centrifugation, resuspended, and bacterial fluorescence (abs/em 465/540) analyzed by plate reader. (**E**) BMDM were treated as in (**D**), fixed, stained for DAPI, and visualized by confocal microscopy. *Left:* Representative image. White arrowheads indicate cytosolic *S. typhiurium* positive for 2-NBDG and DAPI. Scale bar 10 μM. *right:* 2-NBDG signal in areas of cytosol negative for DAPI (*S. typhimurium* negative) was measured. Cytosolic regions from ~200 discrete cells from 4 fields of view were measured per condition. Error bars represent mean +/- sd of different fields of view. (**F**) BMDMs were infected with stationary phase *S. typhimurium* and analyzed for cytosolic NAD+/NADH. ΔNAD+/NADH indicates the difference between the ratio measured at 11hr and 5hr post-infection. (**G**) BMDMs were infected with stationary phase *S. typhimurium* and levels of lactate in the supernatant analyzed at the indicated timepoints. (**H**) Quantification of the difference between lactate secretion measured at 11hr and 5hr post-infection.

Figure 9. Disruption of glycolysis by *Salmonella typhimurium* activates the NLRP3 inflammasome. (A-D) BMDMs were infected with *S. typhimurium* grown to stationary phase in the presence or absence of 1 mM pyruvate and (**A**) cells were fixed and stained for ASC and DAPI. ASC foci/nuclei were quantified. At least four fields of view (~2000 cells) were analyzed per condition. (**B**) IL-1β secretion was analyzed by ELISA, (**C**) Cell death was measured by LDH release. (**D**) Representative image from (**A**). White arrowheads indicate inflammasome foci. Scale bar 30 μm. (**E**) BMDM of the indicated genetic backgrounds were infected with stationary phase *S. typhimurium* (100:1 MOI) in the presence or absence of pyruvate. Inflammasome foci were quantified at 17hr post-infection. (**F**) BMDMs were infected with stationary phase *S.*

typhimurium 12023 (25:1) expressing a replication plasmid. Generations were quantified at the indicated timepoints post-infection. Data are representative of n=3 experiments. (**G**) BMDMs were infected with stationary phase *S. typhimurium* 12023 (100:1 MOI) constitutively expressing EGFP. Cells were fixed at 17hr post-infection, stained for ASC, and infection visualized by confocal microscopy. Scale bar 15 μm. (**H**) Minimal medium containing vehicle, 2 mM glucose, or 2 mM pyruvate was inoculated with wildtype *S. typhimurium*. Bacterial growth was measured by analyzing OD_{600}. (**I**) Cytosolic NAD+/NADH was analyzed at 5 and 11hr post infection with *S. typhimurium* (100:1 MOI) or vehicle (uninf.) in the presence or absence of 1 mM pyruvate (pyr). NAD+ consumption rate indicates the difference in NAD+/NADH ratio between 5 and 11hr post-infection. Data are representative of n=3 experiments. For LDH release, ELISA, and metabolic assays, error bars indicate mean +/- sd of technical triplicate. Data were analyzed for statistical significance using an unpaired, two-tailed t test.

Figure 9 – figure supplement 1. Pyruvate prevents *S. typhimurium*-induced inflammasome formation in a dose-dependent manner. (**A**) BMDM were infected with stationary phase *S. typhimurium* in the presence of increasing concentrations of pyruvate and inflammasome foci quantified. (**B**) BMDM were infected with ΔorgA (SPI-1 deficient) *S. typhimurium* grown to stationary phase at 25:1 MOI in the presence or absence of 1 mM pyruvate. Inflammasome foci were quantified at 14hr post-infection.

Figure 9 – figure supplement 2. Inflammasome formation and cell death induced by log phase *S. typhimurium* infection are unaffected by pyruvate. (**A**) BMDM were infected with *S. typhimurium* grown to log phase (10:1 MOI) in the presence or absence of pyruvate and

inflammasome foci were quantified. (**B**) BMDMs were treated as in (**A**) and cell death was quantified by LDH release.

Figure 10. Model of NLRP3 inflammasome activation induced by disruption of glycolytic flux. *S. typhimurium* and chemical inhibitors disrupt glycolytic flux in LPS-primed BMDM, resulting in an increase in NAD+/NADH, a decrease in ATP production, and a decrease in lactate secretion. TCA cycle metabolism is also impaired, potentiating the elevated NAD+/NADH ratio into the mitochondria. Mitochondrial ROS are produced by glycolytic disruption and trigger NLRP3 inflammasome formation, IL-1β production, and pyroptosis.

Supplementary file 1. Complete MudPIT dataset. BMDM from four different treatment conditions (see Figure 2) were lysed and lysates reacted with alkyne-biotin. Biotin-labeled proteins were enriched using streptavidin resin, digested off the resin, and bound proteins identified by mass spectrometry. Number of spectral counts from peptides from each identified protein are reported for each condition.

Supplementary file 2. Complete MudPIT dataset normalized to endogenously biotinylated proteins. Data from Supplementary file 1 was normalized based on relative abundance of endogenously biotinylated proteins across conditions. This data reports normalized spectral counts.

Supplementary file 3. Hits from MudPIT analysis. A protein was selected as a 'hit' if, in Supplementary file 2, it had over 30 spectral counts in Condition 1, showed 80% competition for az-GB binding by GB111 (Condition 2), and showed <50% competition for az-GB binding by

GB-IA (Condition 3). The proteins meeting these criteria and number of spectral counts in each condition are shown.

Supplementary file 4: Compound Characterization and Spectra.

Figure 1

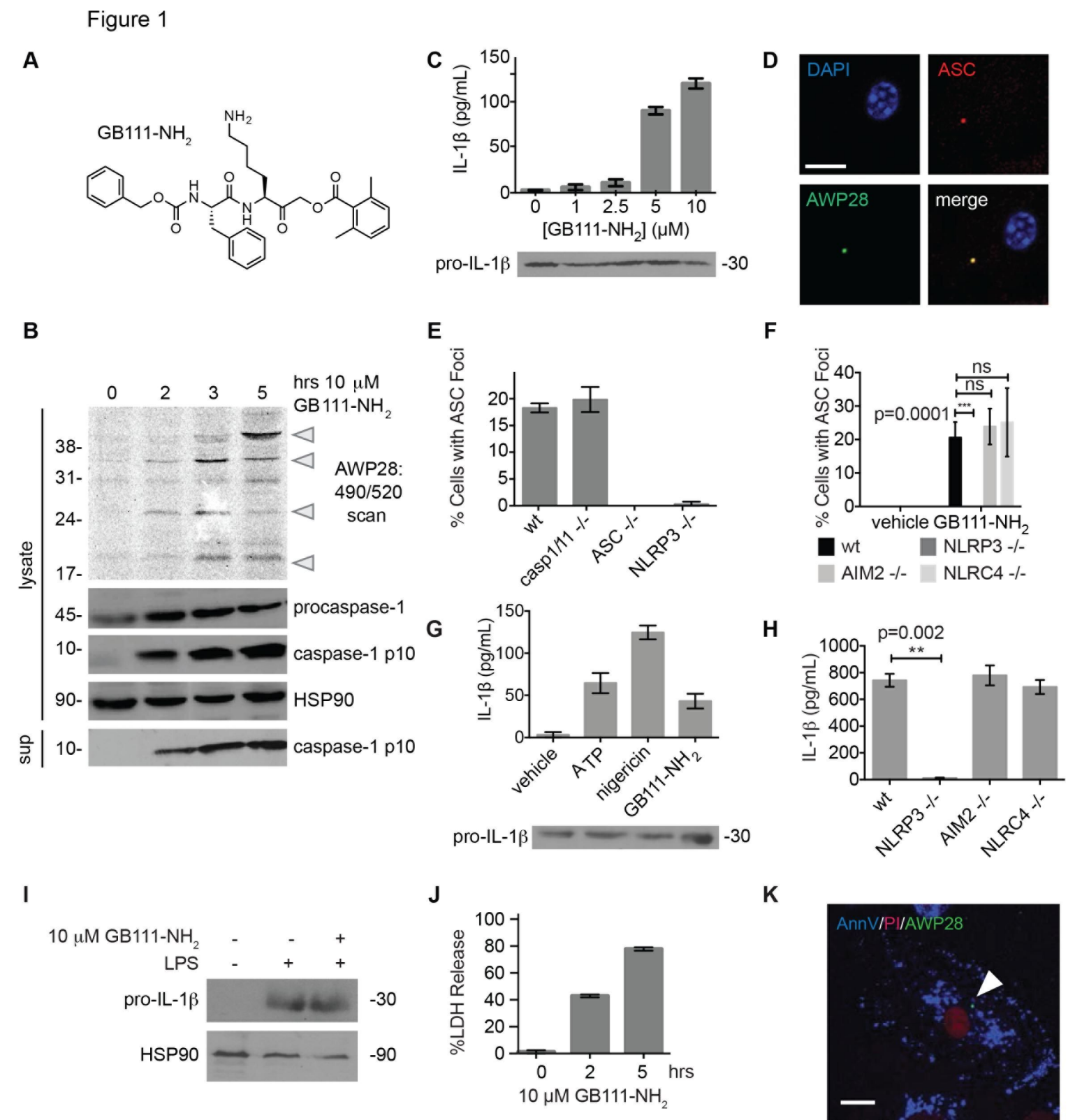
A
GB111-NH2
NH2
B
0
2
3
5
hrs 10 μM GB111-NH2
38-
31-
24-
17-
AWP28: 490/520 scan
lysate
45-
procaspase-1
10-
caspase-1 p10
90-
HSP90
sup
10-
caspase-1 p10
C
IL-1β (pg/mL)
150
100
50
0
0
1
2.5
5
10
[GB111-NH2] (μM)
pro-IL-1β
-30
D
DAPI
ASC
AWP28
merge
E
% Cells with ASC Foci
20
15
10
5
0
wt
casp1/11 -/-
ASC -/-
NLRP3 -/-
F
% Cells with ASC Foci
40
30
20
10
0
ns
ns
***
p=0.0001
vehicle GB111-NH2
wt
NLRP3 -/-
AIM2 -/-
NLRC4 -/-
G
IL-1β (pg/mL)
150
100
50
0
vehicle
ATP
nigericin
GB111-NH2
pro-IL-1β
-30
H
p=0.002
**
IL-1β (pg/mL)
1000
800
600
400
200
0
wt
NLRP3 -/-
AIM2 -/-
NLRC4 -/-
I
10 μM GB111-NH2
-
-
+
LPS
-
+
+
pro-IL-1β
-30
HSP90
-90
J
%LDH Release
100
80
60
40
20
0
0
2
5
hrs
10 μM GB111-NH2
K
AnnV/PI/AWP28

Figure 2

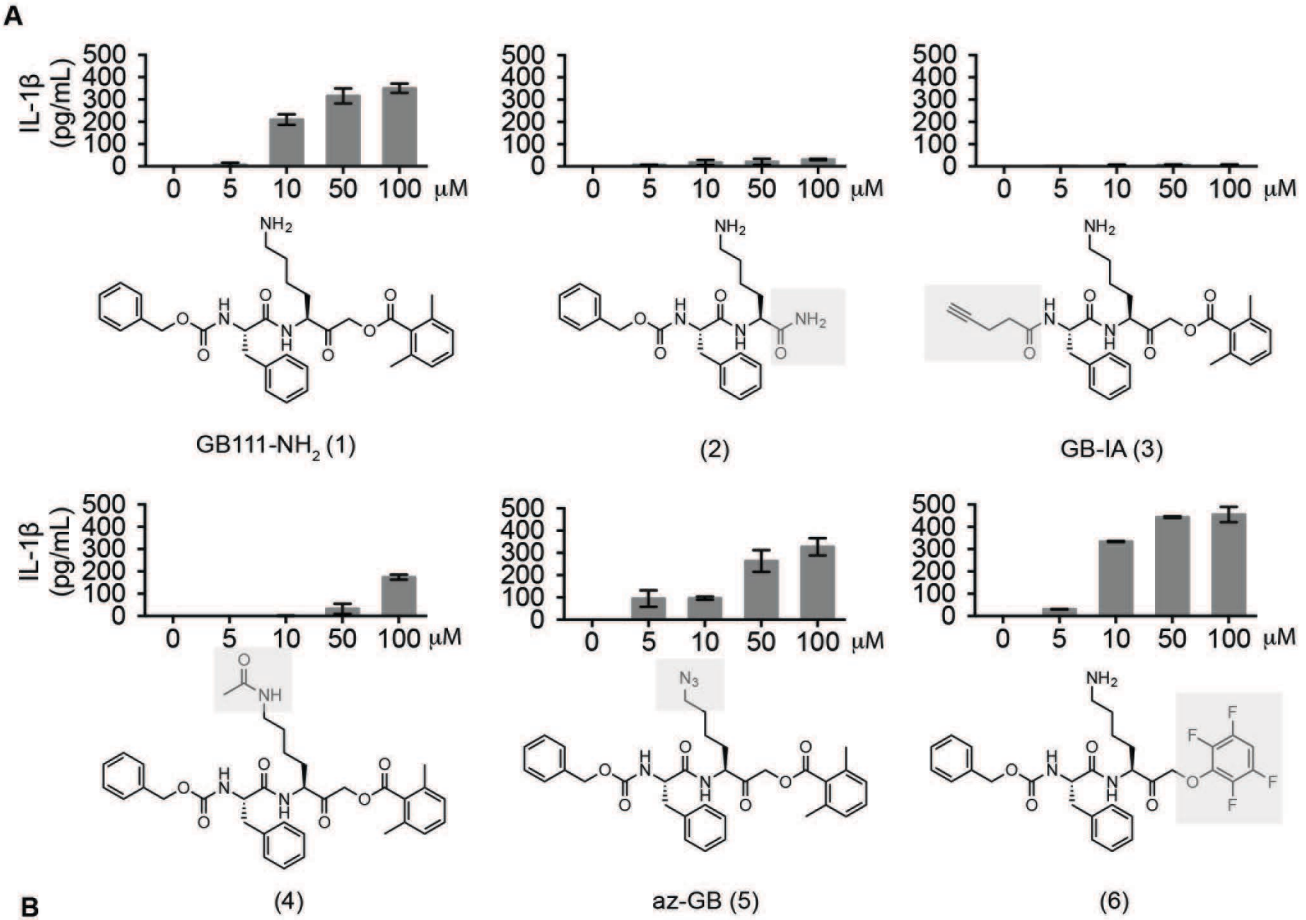

B

Condition	pretreat →	treat →	biotin alkyne Click →	candidate protein
1	DMSO	az-GB **(5)**		present
2	GB111-NH_2 **(1)**	az-GB **(5)**		baseline
3	GB-IA **(3)**	az-GB **(5)**		present
4	DMSO	DMSO		baseline

Figure 3

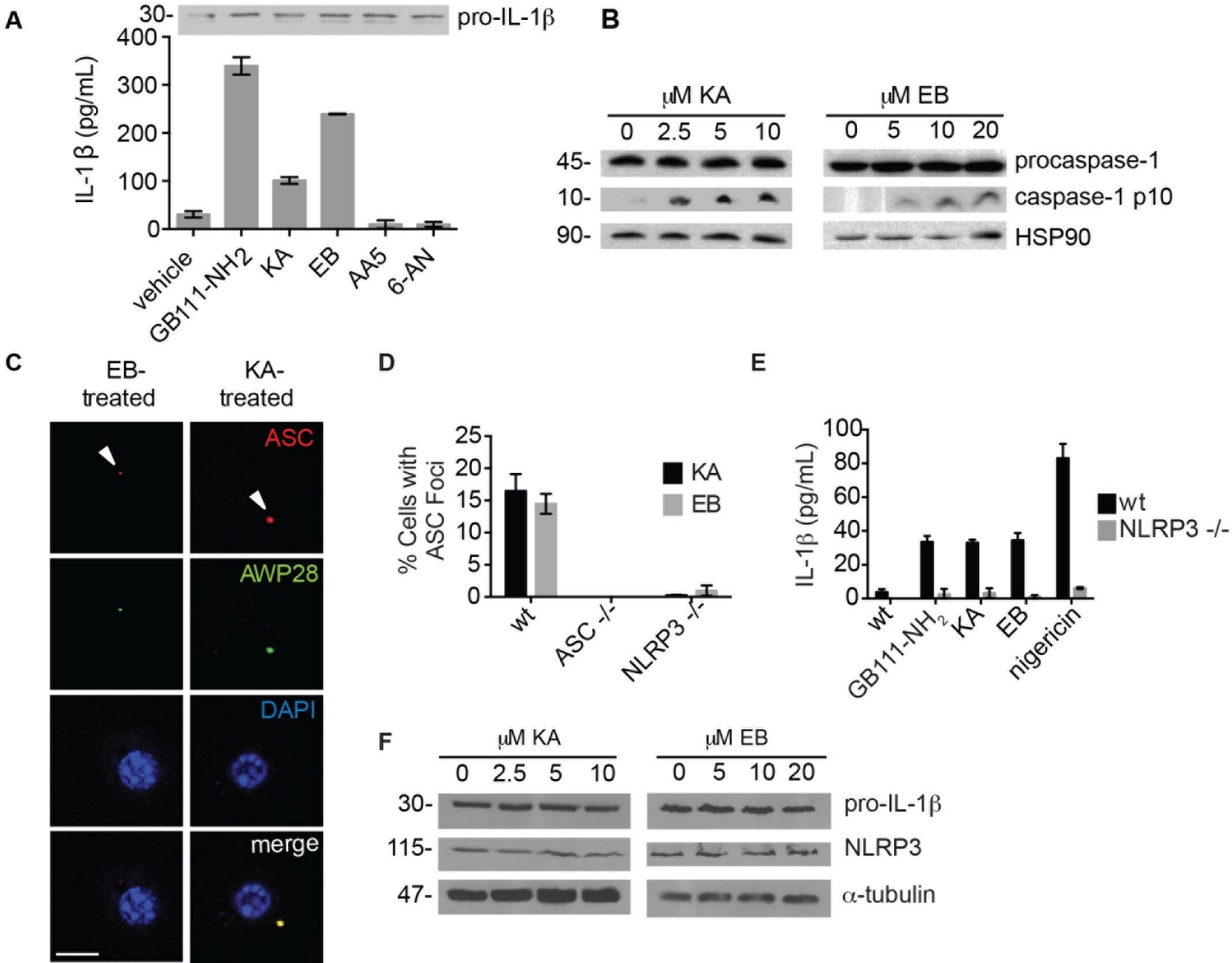
A
30-
pro-IL-1β
IL-1 β (pg/mL)
400
300
200
100
0
vehicle
GB111-NH2
KA
EB
AA5
6-AN
B
μM KA
0 2.5 5 10
μM EB
0 5 10 20
45-
10-
90-
procaspase-1
caspase-1 p10
HSP90
C
EB-treated
KA-treated
ASC
AWP28
DAPI
merge
D
% Cells with ASC Foci
25
20
15
10
5
0
KA
EB
wt
ASC -/-
NLRP3 -/-
E
IL-1β (pg/mL)
100
80
60
40
20
0
wt
NLRP3 -/-
wt
GB111-NH2
KA
EB
nigericin
F
μM KA
0 2.5 5 10
μM EB
0 5 10 20
30-
115-
47-
pro-IL-1β
NLRP3
α-tubulin

Figure 4

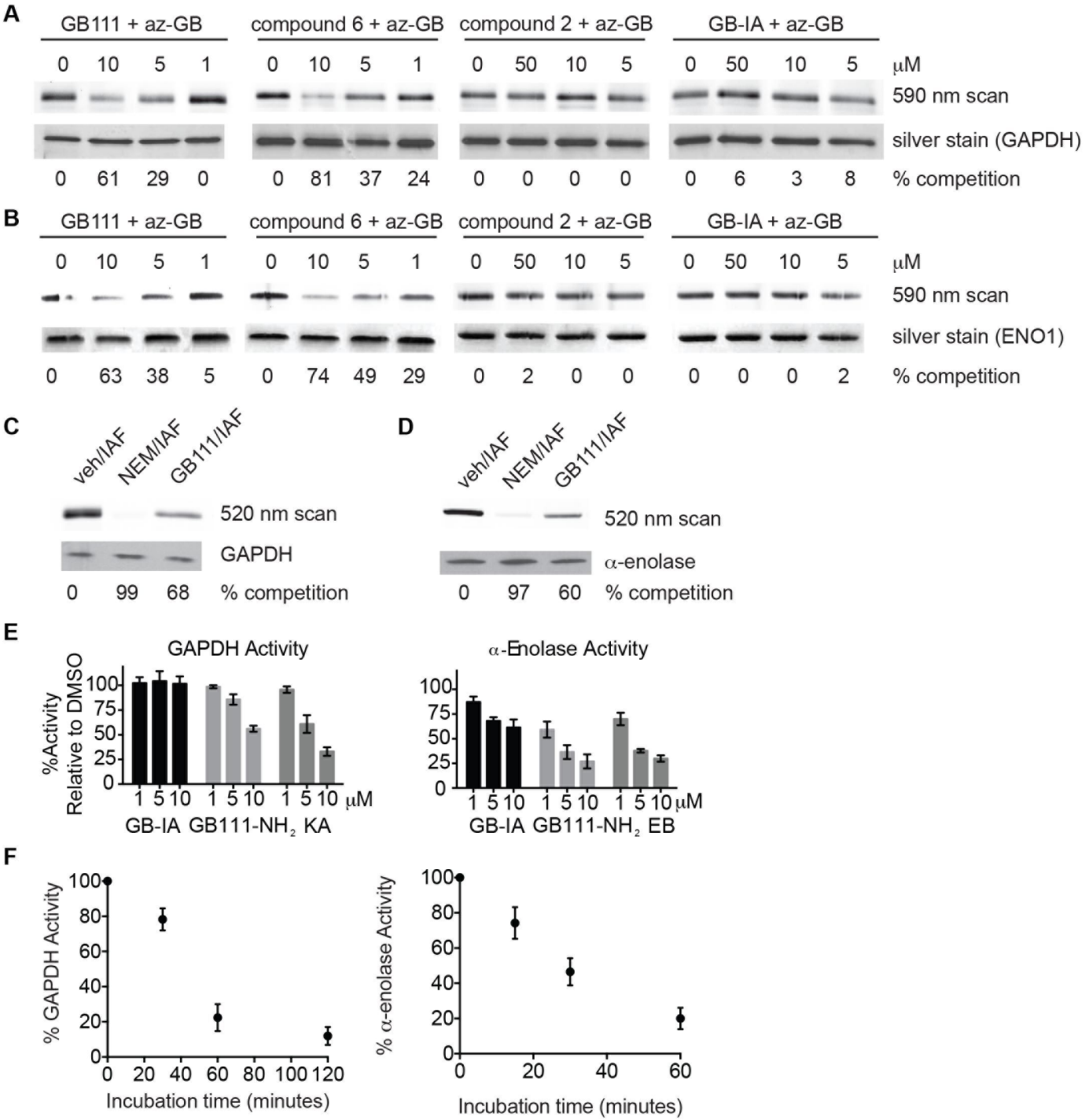
A
GB111 + az-GB
compound 6 + az-GB
compound 2 + az-GB
GB-IA + az-GB
0 10 5 1
0 10 5 1
0 50 10 5
0 50 10 5
μM
590 nm scan
silver stain (GAPDH)
0 61 29 0
0 81 37 24
0 0 0 0
0 6 3 8
% competition
B
GB111 + az-GB
compound 6 + az-GB
compound 2 + az-GB
GB-IA + az-GB
0 10 5 1
0 10 5 1
0 50 10 5
0 50 10 5
μM
590 nm scan
silver stain (ENO1)
0 63 38 5
0 74 49 29
0 2 0 0
0 0 0 2
% competition
C
veh/IAF
NEM/IAF
GB111/IAF
520 nm scan
GAPDH
0 99 68 % competition
D
veh/IAF
NEM/IAF
GB111/IAF
520 nm scan
α-enolase
0 97 60 % competition
E
GAPDH Activity
%Activity Relative to DMSO
100
75
50
25
0
1 5 10 1 5 10 1 5 10 μM
GB-IA GB111-NH2 KA
α-Enolase Activity
100
75
50
25
0
1 5 10 1 5 10 1 5 10 μM
GB-IA GB111-NH2 EB
F
% GAPDH Activity
100
80
60
40
20
0
0 20 40 60 80 100 120
Incubation time (minutes)
% α-enolase Activity
100
80
60
40
20
0
0 20 40 60
Incubation time (minutes)

Figure 5

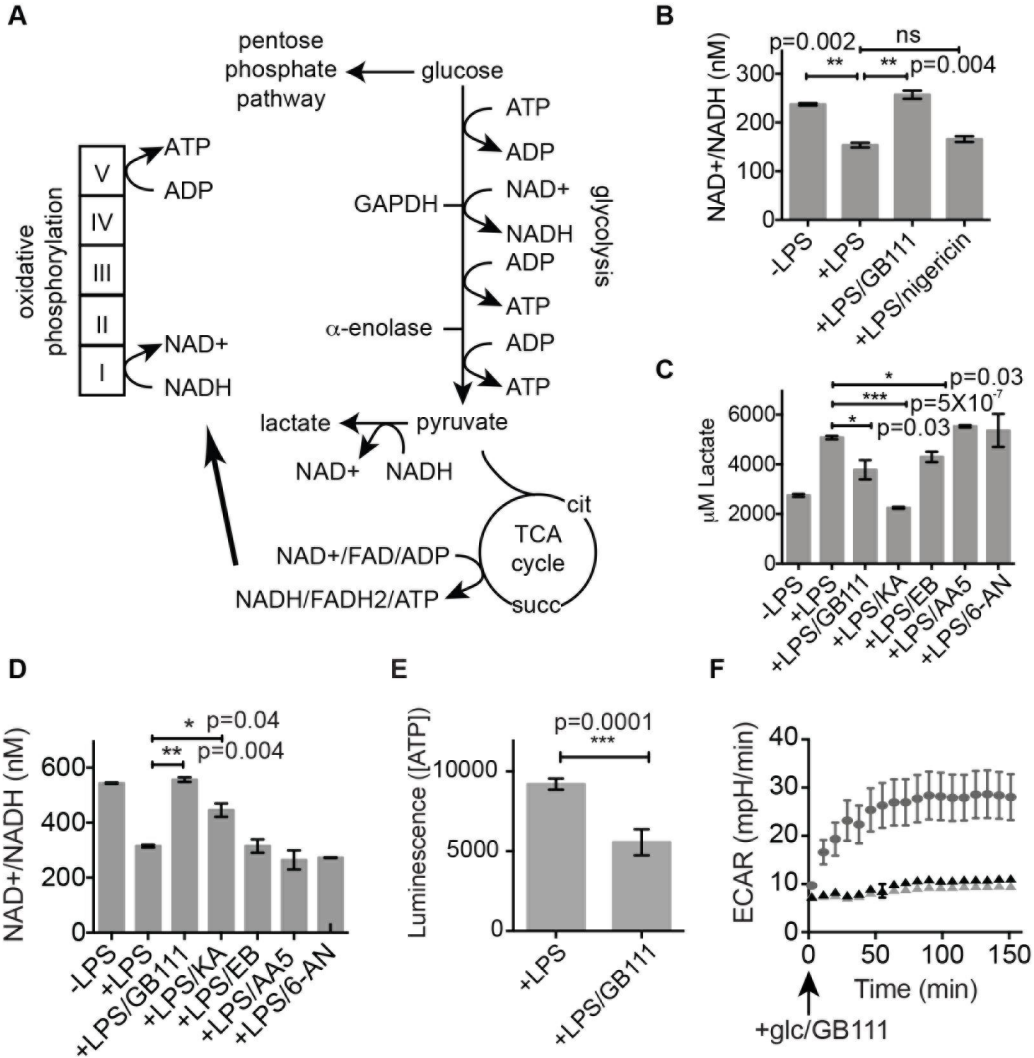
A
pentose phosphate pathway
glucose
ATP
ADP
GAPDH
NAD+
NADH
glycolysis
α-enolase
lactate
pyruvate
cit
TCA cycle
succ
NAD+/FAD/ADP
NADH/FADH2/ATP
oxidative phosphorylation
V
IV
III
II
I
B
NAD+/NADH (nM)
p=0.002
ns
p=0.004
-LPS
+LPS
+LPS/GB111
+LPS/nigericin
C
μM Lactate
p=0.03
p=5X10-7
p=0.03
-LPS
+LPS
+LPS/GB111
+LPS/KA
+LPS/EB
+LPS/AA5
+LPS/6-AN
D
NAD+/NADH (nM)
p=0.04
p=0.004
E
Luminescence ([ATP])
p=0.0001
+LPS
+LPS/GB111
F
ECAR (mpH/min)
Time (min)
+glc/GB111

Figure 6

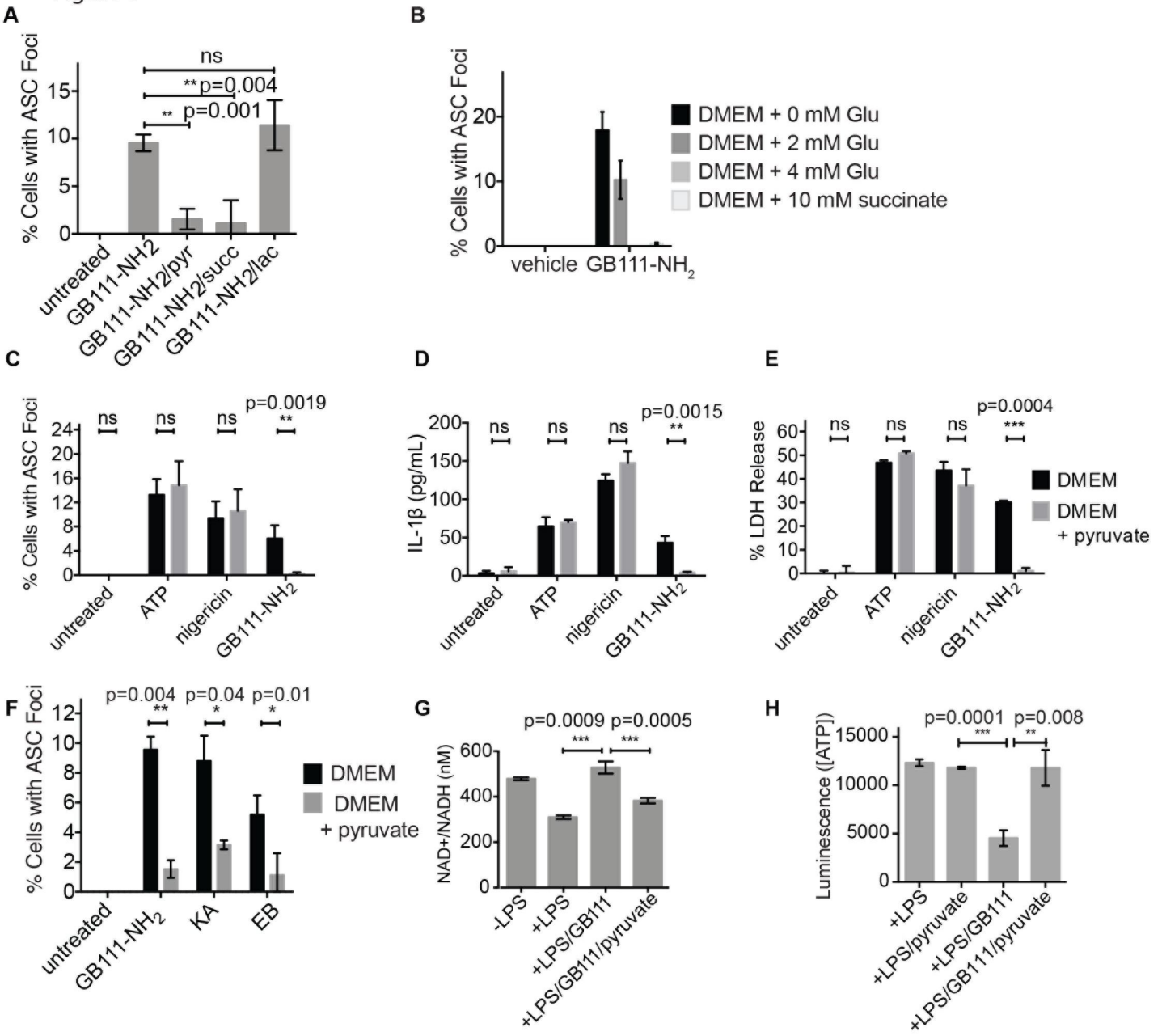
A
% Cells with ASC Foci
ns
**p=0.004
** p=0.001
untreated
GB111-NH2
GB111-NH2/pyr
GB111-NH2/succ
GB111-NH2/lac
B
% Cells with ASC Foci
DMEM + 0 mM Glu
DMEM + 2 mM Glu
DMEM + 4 mM Glu
DMEM + 10 mM succinate
vehicle
GB111-NH2
C
% Cells with ASC Foci
p=0.0019
untreated
ATP
nigericin
GB111-NH2
D
IL-1β (pg/mL)
p=0.0015
E
% LDH Release
p=0.0004
DMEM
DMEM + pyruvate
F
% Cells with ASC Foci
p=0.004
p=0.04
p=0.01
KA
EB
G
NAD+/NADH (nM)
p=0.0009
p=0.0005
-LPS
+LPS
+LPS/GB111
+LPS/GB111/pyruvate
H
Luminescence ([ATP])
p=0.0001
p=0.008
+LPS/pyruvate

Figure 7

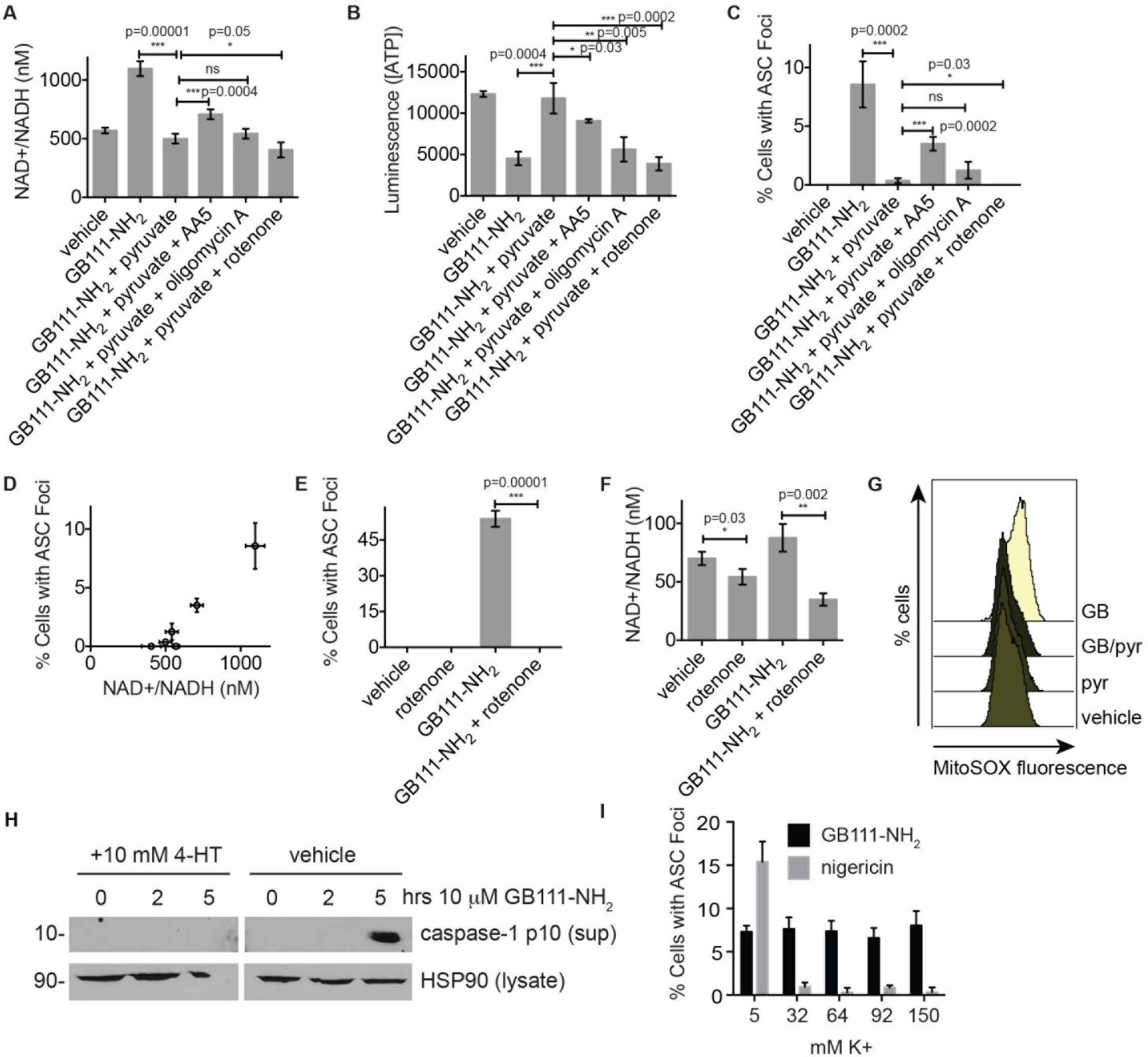
A
NAD+/NADH (nM)
p=0.00001
p=0.05
ns
p=0.0004
vehicle
GB111-NH2
GB111-NH2 + pyruvate
GB111-NH2 + pyruvate + AA5
GB111-NH2 + pyruvate + oligomycin A
GB111-NH2 + pyruvate + rotenone
B
Luminescence ([ATP])
p=0.0002
p=0.005
p=0.03
p=0.0004
C
% Cells with ASC Foci
p=0.0002
p=0.03
ns
p=0.0002
D
% Cells with ASC Foci
NAD+/NADH (nM)
E
% Cells with ASC Foci
p=0.00001
vehicle
rotenone
GB111-NH2
GB111-NH2 + rotenone
F
NAD+/NADH (nM)
p=0.03
p=0.002
G
% cells
GB
GB/pyr
pyr
vehicle
MitoSOX fluorescence
H
+10 mM 4-HT
vehicle
0 2 5 0 2 5 hrs 10 μM GB111-NH2
10-
caspase-1 p10 (sup)
90-
HSP90 (lysate)
I
% Cells with ASC Foci
GB111-NH2
nigericin
5 32 64 92 150
mM K+

Figure 8

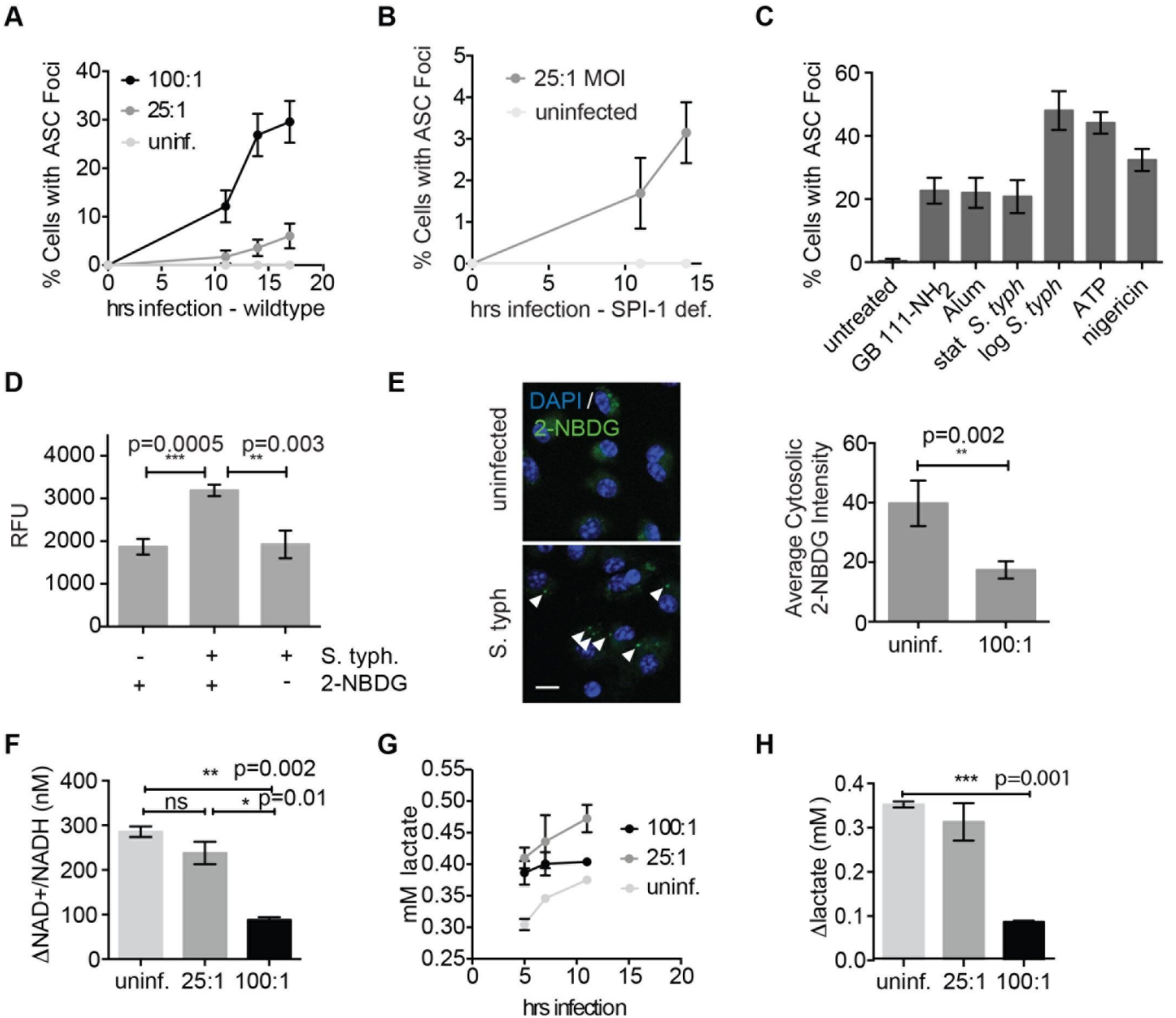
A
% Cells with ASC Foci
100:1
25:1
uninf.
hrs infection - wildtype
B
% Cells with ASC Foci
25:1 MOI
uninfected
hrs infection - SPI-1 def.
C
% Cells with ASC Foci
untreated
GB 111-NH2
Alum
stat S. typh
log S. typh
ATP
nigericin
D
RFU
p=0.0005
***
p=0.003
**
S. typh.
2-NBDG
E
uninfected
S. typh
DAPI /
2-NBDG
Average Cytosolic 2-NBDG Intensity
p=0.002
**
uninf.
100:1
F
ΔNAD+/NADH (nM)
** p=0.002
ns
* p=0.01
uninf.
25:1
100:1
G
mM lactate
100:1
25:1
uninf.
hrs infection
H
Δlactate (mM)
*** p=0.001
uninf.
25:1
100:1

Figure 9

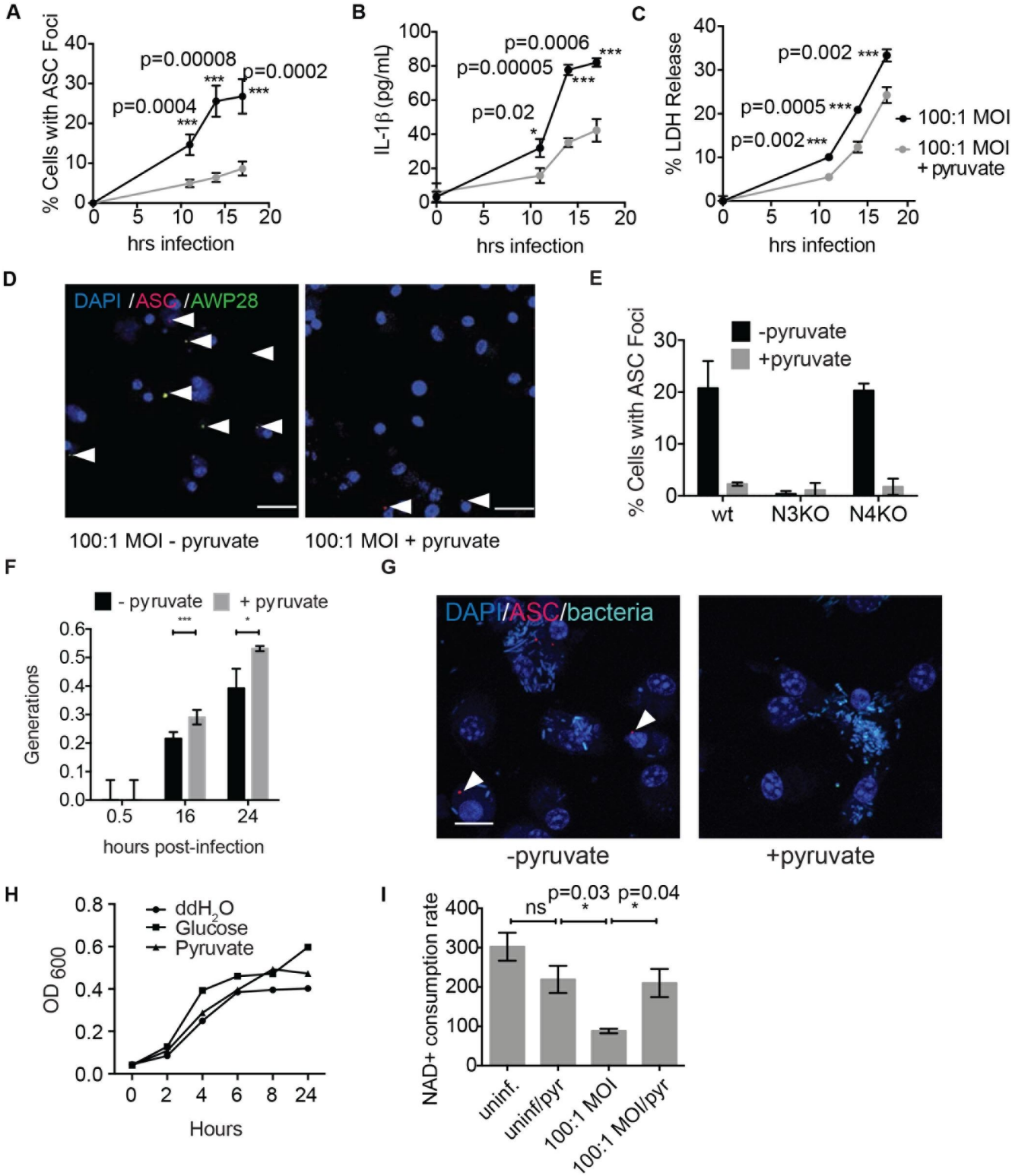
A
% Cells with ASC Foci
hrs infection
p=0.00008
p=0.0004
p=0.0002
B
IL-1β (pg/mL)
hrs infection
p=0.0006
p=0.00005
p=0.02
C
% LDH Release
hrs infection
p=0.002
p=0.0005
p=0.002
100:1 MOI
100:1 MOI + pyruvate
D
DAPI /ASC /AWP28
100:1 MOI - pyruvate
100:1 MOI + pyruvate
E
% Cells with ASC Foci
-pyruvate
+pyruvate
wt
N3KO
N4KO
F
- pyruvate
+ pyruvate
Generations
hours post-infection
G
DAPI/ASC/bacteria
-pyruvate
+pyruvate
H
ddH2O
Glucose
Pyruvate
OD 600
Hours
I
NAD+ consumption rate
ns
p=0.03
p=0.04
uninf.
uninf/pyr
100:1 MOI
100:1 MOI/pyr

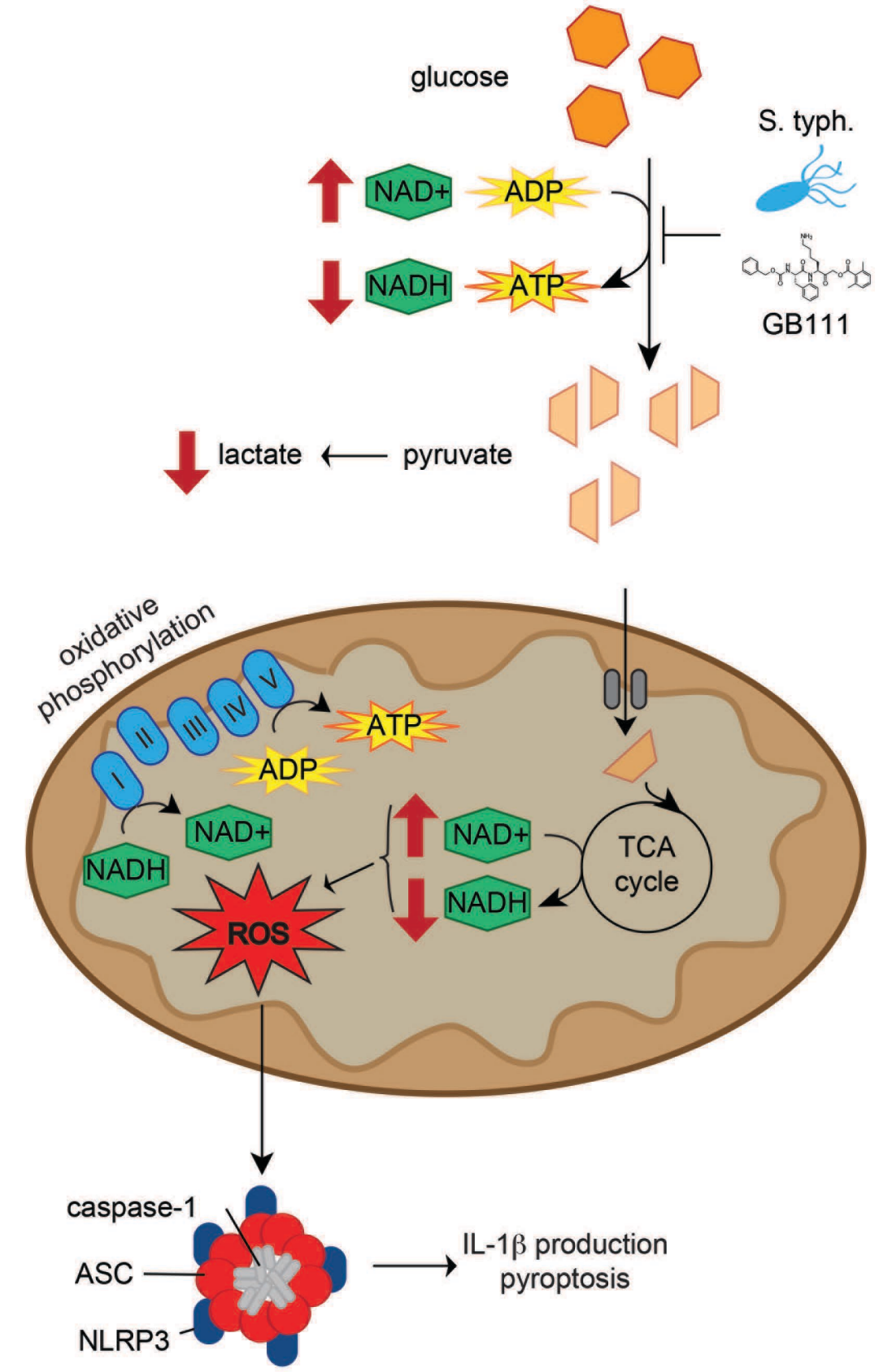
glucose
S. typh.
NAD+
ADP
NADH
ATP
GB111
lactate
pyruvate
oxidative phosphorylation
I
II
III
IV
V
ATP
ADP
NAD+
NADH
NAD+
NADH
TCA cycle
ROS
caspase-1
ASC
NLRP3
IL-1β production
pyroptosis